WATER RESOURCES RESEARCH, VOL. 33, NO. 5, PAGES 971–990, MAY 1997

# Ground-penetrating-radar-assisted saturation and permeability estimation in bimodal systems

Susan S. Hubbard

Department of Civil and Environmental Engineering, University of California, Berkeley

Earth Science Division, Lawrence Berkeley National Laboratory, Berkeley, California

Yoram Rubin

Department of Civil and Environmental Engineering, University of California, Berkeley

Ernie Majer

Earth Science Division, Lawrence Berkeley National Laboratory, Berkeley, California

**Abstract.** Near-surface investigations often require characterization of vadose zone hydraulic parameters. Conventional sampling or borehole techniques for estimating these parameters are costly, time consuming, and invasive, all of which limit collection of hydrogeological data at a spacing needed for detailed site characterization. Incorporation of two- or three-dimensional densely sampled geophysical data with conventional hydrological data increases the amount of data available for the characterization and thus has the potential to significantly improve the hydraulic parameter estimates over those obtained from borehole data alone. The hydraulic estimation procedure can be greatly improved by incorporating dielectric information potentially available from ground penetrating radar (GPR), a noninvasive, high-resolution geophysical method. The procedures for collecting and processing GPR data in the format needed for the proposed estimation technique are relatively new and still a topic of research; our method requires as a starting point the ability to estimate dielectric constants from GPR data. Numerical experiments were performed to investigate the general utility of the GPR-assisted estimation technique under a range of conditions. Three bimodal systems were investigated, each system being composed of a sand facies together with another facies with a larger clay volume fraction; each facies was defined using characteristic values of clay content, porosity, and permeability. Using dielectric information and petrophysical relations, degree of saturation and intrinsic permeability values at each location within the three systems were identified. For bimodal systems, a dielectric constant measurement corresponds to two possible values of saturation and intrinsic permeability at each location; single values of saturation and intrinsic permeability were estimated from these values using the principle of maximum likelihood. Results from case studies demonstrate that a combination of GPR data with conventional borehole data significantly improves the estimates of saturation and has the potential to improve the estimates of permeability over those obtained from well bore data alone. The proposed method should be especially advantageous for vadose zone characterization in areas favorable for GPR data acquisition, where detailed hydraulic parameter information is required but the drilling of numerous boreholes is prohibited.

## 1. Introduction

Near-surface environmental, agricultural, and engineering investigations often require detailed characterization of vadose zone hydraulic parameters. Estimates of hydraulic conductivity are needed to model and predict pollutant transport through the subsurface and to subsequently design an efficient and reliable remediation plan. Soil water content monitoring is important, for example, to maintain an optimal balance between crop yield and groundwater pumping [*Topp et al*., 1980], for flood control [*Topp et al*., 1980], to maintain ecosystem harmony [*Schlesinger et al*., 1990], and to maintain proper moisture in highway subgrades [*Birchak et al*., 1974]. Hydraulic conductivity is estimated from core samples in the laboratory, and field saturated hydraulic conductivity in the vadose zone is commonly estimated using an infiltrometer or a borehole permeameter [*Elrick and Reynolds*, 1992; *Green and Topp*, 1992]. Soil water content can be measured using laboratory gravimetric, laboratory gamma ray attenuation, borehole resistance, borehole capacitance, borehole neutron probe, and time-domain reflectrometry techniques [*Kutilek and Nielson*, 1994]. These laboratory or downhole methods are costly, time-consuming, and invasive, all of which limit our ability to estimate the distribution of the hydrogeologic parameters needed for detailed site characterization. Additionally, the "support scale" sampled by some of these techniques may not be compatible with the scale of the effective parameters that control fluid migration through the system. Thus there is a need for a



Paper number 96WR03979.
0043-1397/97/96WR-03979$09.00

noninvasive technique that can capture spatial variations in hydraulic parameters at a scale appropriate for site characterization.

Numerous inverse methods have been proposed to estimate the spatial distribution of hydraulic parameters [see reviews by *Yeh*, 1986; *Ginn and Cushman*, 1990; *Sun*, 1994]. Stochastic methods focus on a probabilistic distribution of the parameters and offer an appropriate estimation approach given a limited amount of field data and the wide range of small-scale hydraulic conductivity values commonly encountered in the field. Increasing the amount of field hydrogeological measurements available for the inverse procedure improves the parameter estimates. Similarly, incorporation of densely sampled geophysical data that can be related to hydraulic parameters has the potential to significantly improve the estimates over those obtained from well bore data alone.

Geophysical data together with borehole information have been used in the petroleum industry for decades to aid in reservoir structural and stratigraphic mapping, as well as material and hydraulic property estimation. Geophysical data can provide dense spatial coverage at different levels of resolution and can sometimes be employed remotely, allowing measurements of undisturbed material while not creating any potential contaminant conduits. These methods include electrical, seismic, gravity, magnetic, and borehole geophysical approaches. The demand for better understanding shallow geology has driven the development of near-surface geophysical methods in the last decade; an excellent compilation of geophysical papers addressing near-surface techniques is given by *Ward* [1990]. The geophysical methods best suited for near-surface investigations operate within a frequency range such that the sample measurement is collected from volumes larger than core samples but smaller than those associated with conventional pumping or injection tests; the vertical resolution associated with this range is often on the order of a few meters or less. The "support scale" offered by these methods lends itself well to near-surface site investigations, enabling a dense geophysical sampling at a scale useful for characterization and also offering the possibility of bridging the gap between core scale and pumping-test scale measurements. Each near-surface investigation has a unique set of challenges and specific goals, and thus the geophysical technique that is most appropriate and cost-effective must be identified on a case-by-case basis. For example, seismic and ground-penetrating radar (GPR) techniques perform optimally under quite different conditions. GPR performs favorably in the absence of electrically conductive materials and thus will experience optimal performance in sandy material in the vadose zone. Seismic methods work best in completely saturated environments, and seismic energy can easily penetrate damp clays that can be good electrical conductors [*Steeples and Miller*, 1990]. Because of the higher frequencies employed, GPR offers better resolution but less penetration than seismic when they are both operating under favorable conditions.

Several studies have advocated the joint use of geophysical and hydrogeological data to estimate aquifer properties. Electrical methods have been used to estimate the hydraulic properties of aquifers; a review of some of these techniques is given by *Mazac et al*. [1985]. *Rubin et al*. [1992a] and *Copty et al*. [1993] presented methods to estimate a hydraulic conductivity field given complete seismic velocity information from crosshole or surface reflection methods, sparse hydraulic conductivity and hydraulic head measurements, and petrophysical relationships that related seismic velocities to hydraulic conductivity. Using a maximum likelihood technique to handle the nonuniqueness between the hydrogeological and geophysical parameters, they showed that even with significant velocity estimation error the hydraulic conductivity field estimate was improved when seismic data were included in the procedure. *Hyndman et al*. [1994] developed an inversion algorithm that uses both seismic cross-well travel times and solute tracer concentrations to estimate interwell geology and hydraulic parameters. Using model data, they showed that their coupled geophysical-hydrogeological method successfully estimated large-scale lithologic geometry, hydraulic conductivities, and small-scale dispersivity. *Copty and Rubin* [1995] developed a formal stochastic approach that combined surface seismic data and well data to estimate the spatial arrangement of lithofacies and their mean hydrogeological parameters. The methods used by *Rubin et al*. [1992a], *Copty et al*. [1993], *Copty and Rubin* [1995], and *Hyndman et al*. [1994] are most appropriate for conditions where seismic techniques perform optimally, such as in a completely saturated system.

The use of joint geophysical-hydrogeological data for parameter estimation in the unsaturated zone has been a focus of several recent investigations. *Mazac et al*. [1988] used regression analysis to relate resistivity measurements to saturated hydraulic conductivity in the zone of aeration where the moisture content was above 30%. *Sheets and Hendrickx* [1995] also used regression techniques to investigate the relationship between total soil water content estimated with borehole neutron probes and the bulk soil electrical conductivity estimated using electromagnetic induction. They demonstrated that surface electromagnetic methods combined with borehole hydrogeological data offer a quick and accurate estimation of soil water content once a site-specific calibration curve between conductivity and soil water content has been developed.

In this study we investigate the joint use of GPR and borehole data for the estimation of vadose zone hydraulic parameters in bimodal systems. In section 2 we present the mathematical statement of the approach in which saturation and the permeability of the facies comprising the system are defined as binary random variables with density functions conditioned on extensive measurements from GPR field data. The procedure for obtaining information from GPR data, including the method of analyzing the radar data and the petrophysical expressions that are used to relate information from GPR data to hydrogeologic parameters, is discussed in section 3. Numerical case studies that demonstrate the potential and limitations of hydraulic parameter estimation in bimodal systems using GPR data are presented in section 4. Results from these numerical experiments suggest that a combination of GPR data with conventional borehole data significantly improves the estimates of saturation and have the potential to improve the estimates of permeability over those obtained from well bore data alone. The intrinsic permeability estimated using the GPR-assisted approach can be scaled to saturated hydraulic conductivity and used with relative hydraulic conductivity relationships and the estimated saturation field to obtain unsaturated hydraulic conductivity estimates.

## 2. Mathematical Statement of the Theoretical Approach: Maximum Likelihood Estimation in the Bimodal Case

For this study we consider a bimodal permeability field, with permeability ($k$) being either $k_1$ or $k_2$. This model is appropriate for geological systems whose components can be cate-

gorized into two groups with distinct permeabilities, such as environments composed of a sand and a clay facies or fractured systems [*Rubin*, 1995]. For example, a bimodal permeability model was used to simulate sand-shale sequences [*Desbarats*, 1987] and also to represent the presence of high- and low-permeability material for inferring the hydrostratigraphy at a site of groundwater contamination [*Johnson and Dreiss*, 1989]. In this study $k_1$ and $k_2$ represent the permeabilities of two facies that comprise a geological system, for example, a clay and a sand facies. In accord with the stochastic approach to site characterization, $k$ is defined as a random function with probability distribution function (pdf):

$$f(k) = P\delta(k - k_1) + (1 - P)\delta(k - k_2) \tag{1}$$

where $\delta$ is the Dirac delta and $P$ is the probability such that

$$k = \begin{cases} k_1 & \text{prob} = P \\ k_2 & \text{prob} = 1 - P. \end{cases} \tag{2}$$

From (1) and (2) we obtain the relation between $P$ and $\langle k \rangle$, where $\langle \quad \rangle$ denotes the expected value operator:

$$P = \frac{\langle k \rangle - k_2}{k_1 - k_2}. \tag{3}$$

Since $P$ is defined from the volume fraction of $k_1$, $\langle k \rangle$ is the unconditional expected value of $k$, and estimates based on (3) and (1) do not account for specific local conditions. In the presence of data other than volumetric fraction, $f(k)$ can be made conditional. Defining $P^c = [P|\{N\}]$ and $\langle k \rangle^c = \langle k|\{N\} \rangle$ as the probability and expected permeability, respectively, conditional on the data set $\{N\}$, the conditional $k$ pdf can be expressed as

$$f^c(k) = P^c\delta(k - k_1) + (1 - P^c)\delta(k - k_2). \tag{4}$$

Note that unlike $P$,

$$P^c = \frac{\langle k \rangle^c - k_2}{k_1 - k_2} \tag{5}$$

is no longer stationary since it depends on the location of the $N$ measurements in the set $\{N\}$. In the Bayesian terminology, $f(k)$ represents the a priori pdf of $k$ while $f^c(k)$ is the a posteriori pdf.

The unconditional and conditional estimation variances for the bimodal distribution are given by:

$$\begin{aligned} \sigma^2 &= (k_1 - k_2)^2 P(1 - P) \\ \sigma^{2,c} &= (k_1 - k_2)^2 P^c(1 - P^c), \end{aligned} \tag{6}$$

respectively. When $\langle k \rangle^c$ in (5) approaches either $k_1$ or $k_2$, $P^c$ approaches 1 or 0, and the conditional estimation variance in (6) approaches zero as the bimodal model reduces to a unimodal, deterministic model.

The maximum likelihood (ML) technique seeks to find model parameter values that render the observed data most probable or "most likely." ML estimators possess several desirable properties such as asymptotic consistency and minimum variance [*Mood and Graybill*, 1963] and have been used by several investigators to estimate hydrogeological parameters [*Kitanidis and Vomvoris*, 1983; *Dagan*, 1985; *Rubin and Dagan*, 1987]. We define the likelihood function $L_k(\underline{x})$:

$$L_k(\underline{x}) = f^c[k(\underline{x})], \tag{7}$$

and on the basis of the ML principle, the ML estimate of $k$ at $\underline{x}$ is the value which maximizes $L_k$. For example, when $\langle k \rangle^c$ is closer to $k_2$ than $k_1$ in (5), the ML estimation of $k(\underline{x})$ is $k_2$.

Under the conditions established in this study, saturation $(S)$ is also defined as a random function with pdf:

$$f(S) = p\,\delta(S - S_1) + (1 - p)\delta(S - S_2). \tag{8}$$

In the unconditional case we have

$$p = P_S = \frac{\langle S \rangle - S_2}{S_1 - S_2} \tag{9}$$

while in the conditional case, $p = P_S^c =$ probability $[S(x) = S_1|\{N\}]$ is defined by

$$P_S^c = \frac{\langle S \rangle^c - S_2}{S_1 - S_2} \tag{10}$$

where $\langle S \rangle^c$ is the conditional mean of $S$. Unlike $k$, which is constrained to two possible values, $S$ in general can take on any value from zero to complete saturation. The bimodality of $S$ presented in (8)–(10) is an outcome of the non-unique relation between dielectric constant and saturation. For a two-facies system, there are two possible permeability values at each location. As dielectric constants can be represented as functions of saturation and permeability using petrophysical relationships, and since we assume that there is one dielectric constant measurement and two possible values of permeability at each location, there are also two possible values of saturation $(S)$ at each location. The dielectric constants change in space due to the presence of two facies in the system as well as to the variability of the saturation; this causes the corresponding values $S_1$ and $S_2$ to vary spatially.

Similar to (7), the likelihood function for estimating saturation is defined as either of these two equations:

$$L_S(\underline{x}) = f[S(\underline{x})] \qquad L_S(\underline{x}) = f^c[S(\underline{x})]. \tag{11}$$

The ML estimate of $S$ at $\underline{x}$ is the value that maximizes $L_S$, and is determined by computing which value ($S_1$ or $S_2$) is closest to the expected value at that location.

The formalism presented so far is not limited to GPR based estimation. The challenge is to define a data set $\{N\}$ that will permit more accurate estimation of either $k$ or $S$. In this paper we focus on the $\{N\}$ which can potentially be obtained from a GPR survey. Obtaining $\{N\}$ from GPR survey data entails estimating the dielectric constant from GPR data and then relating these estimates to hydrogeological parameters using petrophysical relationships. $\{N\}$ can be expanded to include data other than GPR, such as direct measurements of permeability and saturation.

In summary, our estimation procedure calls for identifying the possible values of permeability and saturation at each location using information from GPR data and petrophysical relationships, and estimating the expected values of $k$ and $S$. Based on the principle of ML, the permeability or saturation value which maximizes the likelihood function is selected as the estimate at that location.

## 3. Ground-Penetrating Radar Methods

GPR methods use short pulses of high-frequency (10–1000 MHz) electromagnetic energy to probe the subsurface. The dielectric constant, or, equivalently, the relative permittivity, is used to describe the electrical properties of many geologic

materials at these high frequencies [*Katsube*, 1974]. GPR performance is often poor in electrically conductive environments such as saturated systems or in systems dominated by the presence of expanding clays. Clays such as smectite and vermiculite are more electrically conductive under similar soil moisture conditions than clays such as kaolinite, gibbsite, and goethite [*Doolittle and Collins*, 1995]. In general, GPR performs better in unsaturated coarse-textured or moderately coarse-textured soils. However, GPR techniques have been successful in both saturated environments [*Knoll et al*., 1991; *Fisher et al*., 1992] and in subsurface environments with substantial nonexpanding clay fractions such as at the Savannah River site in South Carolina [*Wyatt et al*., 1996]. The suitability of using GPR for a particular application is not totally clear [*Annan and Cosway*, 1992] and is, as with all geophysical methods, dependent on the soil conditions. In this paper we address the potential of estimating hydrogeological information using dielectric constants obtained from GPR data under a range of saturation conditions and in systems composed of varying amounts of clay. The variations in electrical properties of clays and their effect on GPR performance are not considered. As a starting point for our method, we assume that the site is amenable to radar sounding. Under these circumstances and at the high frequencies used for field radar acquisition, the dependency of radar velocity on electrical conductivity is negligible and the radar signal velocity ($V$) can be related to the real part of the dielectric constant ($\kappa$) as [*Davis and Annan*, 1989]

$$\kappa \approx (c/V)^2 \tag{12}$$

where $c$ is the plane wave propagation velocity of electromagnetic waves in free space ($3 \times 10^{-8}$ m/s). This relationship enables the estimation of the dielectric constants from GPR signal propagation velocities.

GPR systems consist of an impulse generator that repeatedly sends a particular voltage and frequency pulse to a transmitting antenna. A signal propagates from the transmitting antenna through the Earth and is reflected, scattered, and attenuated; a modified signal is subsequently recorded by the receiving antenna. Under conditions where GPR data acquisition is favorable, the GPR signal is primarily altered where there are changes in the dielectric properties of the material, which may be caused by variations in saturation, material constituency, temperature, porosity, and pore fluid composition. The value of $\kappa$ for water is 80 and for air is 1; typical values for common geologic materials range from 3 to 40 [*Davis and Annan*, 1989].

This relatively new geophysical tool has become increasingly popular where there is the need to better understand near-surface conditions. Common uses of GPR data include mapping the top of bedrock as well as locating objects whose electrical properties are different than that of the host environment, such as buried storage tanks. GPR data has been used in hydrogeological investigations to locate the water table and to delineate shallow, unconsolidated aquifers [*Beres and Haeni*, 1991]. Additionally, *Ulriksen* [1982] observed a relation between GPR amplitude power reflection coefficients and water content in the laboratory. He showed, under laboratory conditions, that information about the vertical distribution of water content can be obtained by using multiple-frequency radar antennas where the higher-frequency signals sample the shallowest, dryer layers and the lower-frequency signals sample the deeper layers that are more saturated. This method may be potentially useful for two-dimensional water content estimation in a field study if other factors that influence the amplitudes (geology, surface coupling, etc.) remain constant or can be compensated for and if relationships between amplitudes and water content are available. To date, very little work has been done to formulate a method of extracting hydrogeological properties from GPR data using techniques appropriate for field-scale investigation, as is proposed in this study.

GPR resolution, defined as the ability of the system to distinguish two signals that are close together in time, varies as a function of frequency. *Davis and Annan* [1989] suggest that for a wet soil, vertical resolution on the order of 7 m is possible using 10-MHz radar antennas, 0.5-m resolution is possible using 100-MHz radar antennas, and less than a centimeter resolution is possible using 1000-MHz radar antennas. Increasing the frequency increases the resolution but decreases the penetration depth. Also affecting the radar signal penetration depths are the radar system performance, reflection properties at boundaries where electrical properties vary, and attenuation, which is controlled by scattering, electrical properties of surface and subsurface materials, and geometrical spreading losses. Generally, one chooses a radar center frequency that yields both sufficient penetration and resolution; for field applications this is often between 50 and 200 MHz. It is, however, possible to collect radar data at the same location using several different frequency antennas. The use of multiple-frequency antennas enables sampling over a greater depth range with optimal resolution for all depths [*Smith and Jol*, 1992].

### 3.1. Estimation of Dielectric Constants From GPR Data

Information about the dielectric structure of the shallow subsurface is potentially available from GPR data acquired with surface common midpoint (CMP) or cross-hole tomographic acquisition geometries. CMP geometry results in gathers of traces where the midpoint between the transmitting and receiving antennas is common to all transmitter-receiver pairs; these data can then be processed using standard seismic data processing routines [*Fisher et al*., 1992; *Wyatt et al*., 1996]. As shown by *Wyatt et al*. [1996], the multiple sampling of a subsurface location by the CMP method and subsequent data processing can result in improved data quality over that collected using conventional radar acquisition geometries. Consequently, the CMP method has the potential to enhance data acquisition in traditionally difficult areas. Cross-hole tomographic GPR techniques transmit direct electromagnetic energy from a transmitting antenna in one borehole to a receiving antenna in another borehole over several transmitting/receiving antenna locations. Both CMP and cross-hole tomographic acquisition geometries result in multiple sampling of the subsurface as a function of distance, which permits estimation of the electromagnetic propagation velocity.

A 200-MHz GPR CMP gather is shown in Figure 1a. The linear events that arrive early in time are the air and direct ground waves; these events are considered noise and are muted during processing. The later, hyperbolic-shaped arrivals represent reflections from boundaries where contrasts in dielectric properties exist. The approximately hyperbolic arrival patterns of the GPR CMP reflections are a function of increasing distance between the transmitter and receiver. Normal-move-out (NMO) velocity corrections involve finding the velocity that best removes the offset dependency of the reflection travel times so that the data can be treated as zero-offset arrivals. A "constant velocity panel" method accomplishes this by allowing visual inspection of a group of several consecutive CMPs where the hyperbolic arrival times have been flattened

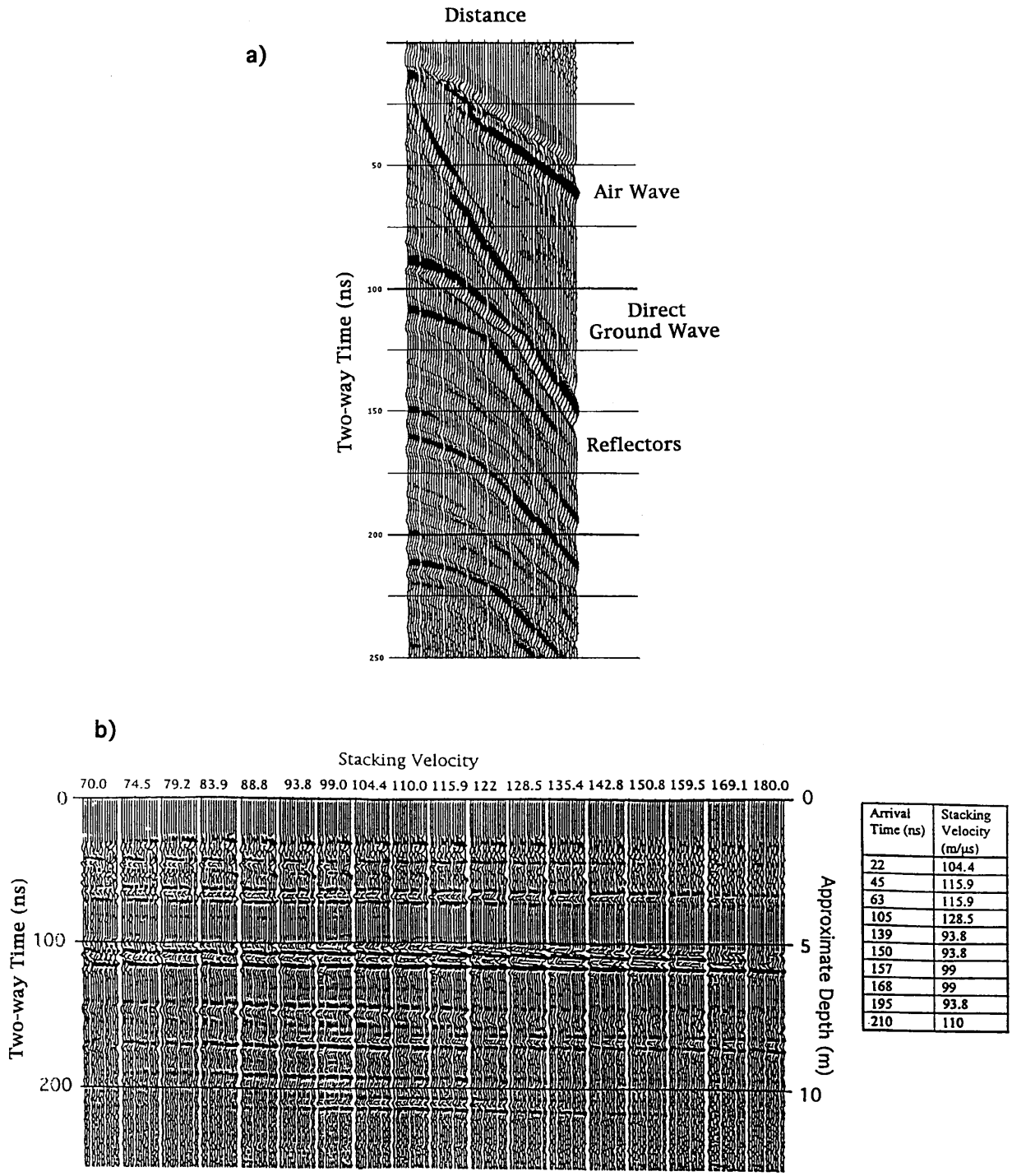


**Figure 1.** (a) A 200-MHz GPR CMP gather. Early linear arrivals are the air and ground waves and later hyperbolic-shaped arrivals are reflections from interfaces that separate soils with different dielectric properties. (b) Constant velocity panel of ground-penetrating radar data. Two-way travel time arrivals from 15 CMPs are stacked with velocities ranging from $70 \times 10^6$ m/s to $180 \times 10^6$ m/s. A one-dimensional stacking velocity function, based on the velocities that produce the highest signal-to-noise ratios for the events, is shown to the right of the panels.

with trial velocities and subsequently summed (stacked) into individual traces [*Yilmaz*, 1987]. The NMO correction with the "correct" velocity function produces a set of traces with the highest signal-to-noise ratio (S/N) when stacked, and that velocity is chosen as the "correct" velocity at the arrival time of the reflection. A velocity versus depth function that yields the best stack response for all times is sought. This NMO method is valid for horizontal subsurface stratigraphy; for dipping layers a process called dip move out (DMO) is more appropriate [*Hale*, 1984]. A constant velocity panel of 200-MHz radar data is shown in Figure 1b, where arrivals from 15 radar CMPs have been moved out and stacked with velocities ranging from 70 $\times$

$10^6$ to $180 \times 10^6$ m/s. A one-dimensional stacking velocity function from analysis of these panels is also shown in Figure 1b. With this particular panel, velocity estimates were obtainable with vertical spacing ranging from 7 to 22 ns (approximately 0.35–2.1 m) with an average spacing of 1 m. This panel also shows that the velocity resolution generally increases with depth; that is, the range of velocities that result in reflections with good S/N after stacking decreases with increasing depth. This is likely due to the fact that the muting process, which is applied to remove the direct and ground waves, results in fewer offsets in the near-surface portion of each stacked trace. Since the S/N generally increases as more offsets are included in the analysis, the near-surface portion of the data has lower S/N and thus less resolution than the deeper portion of the data. The velocity estimates determined using the constant velocity panel method or other velocity analysis methods [*Yilmaz*, 1987] can be converted to interval velocity estimates, or the average velocities in an interval between two reflectors, using the *Dix* [1955] equation. If a grid of evenly spaced velocities is desired, the velocities can be obtained where the S/N is good and then estimated between these values using, for example, linear interpolation or kriging techniques.

For the inversion of cross-hole radar data, the interwell area is discretized into nodes and an attempt is made to determine the value of velocity at each node such that the difference between the observed data and the data calculated for a ray path passing through several nodes is a minimum for all ray paths [*Sena and Toksoz*, 1990; *Nekut*, 1994]. The procedures for collecting and processing GPR data in the format necessary for velocity estimation are relatively new and are still topics of research. Nonetheless, the increase in use of radar data for detailed site investigation suggests that CMP or cross-hole tomographic GPR data acquisition and processing for velocities will become standardized in the future. Obtaining information about radar propagation velocity is a significant benefit of using CMP or cross-hole tomographic GPR recording geometries, as the interval velocity can be related to the dielectric constant of the material using (12). The estimated dielectric constant can then be related to hydraulic properties of the material, as discussed in the following section.

### 3.2. Relation Between Dielectric and Hydrogeologic Parameters

Petrophysical models are necessary to link dielectric estimates from GPR data to hydrogeologic parameters. Several studies have investigated the relationship between dielectric constants and moisture content to enable moisture content estimation from time domain reflectrometry (TDR) measurements. TDR involves use of a metal-pronged field tool that is inserted into the ground and connected to an electromagnetic source and a recording instrument. From the signal travel time and the known prong length, an effective electromagnetic wave propagation velocity over the length of the prongs can be determined and related to the dielectric constant. The dielectric-moisture content relationships have been investigated using both empirical and theoretical approaches. For example, regression analysis was used by *Topp et al*. [1980] to obtain a third-order polynomial which related dielectric constant measurements of soils with a range of textures and densities to volumetric water content. Relationships between dielectric and hydraulic parameters can also be represented using mixture formulae which express the bulk dielectric constant in terms of parameters such as volume fractions and dielectric constants of the individual components, measurement frequency, grain shape, porosity, pore fluid composition, and the relation of the direction of material layering compared to that of the applied electric field. A review of some of the mixture formulae is given by *Shen et al*. [1985]. *Roth et al*. [1990] used a mixture formula to relate dielectric constant measurements obtained from TDR readings to water content, where the bulk dielectric constant of a material was expressed in terms of the dielectric constants of the individual constituents, water saturation and porosity. The mixture formula of *Roth et al*. [1990] and regression relationship of *Topp et al*. [1980] are widely used in soil physics studies to relate TDR measurements of dielectric constants to water content.

*Wharton et al*. [1980] also used a mixture formula to express the bulk dielectric constant as a function of the dielectric constants of air ($\kappa_a$), water ($\kappa_w$), sand ($\kappa_s$), and clay ($\kappa_{cl}$), as well as the porosity ($\phi$), fractional water saturation ($S_w$), and the volumetric clay fraction ($V_{cl}$):

$$\kappa = [(1 - \phi)V_{cl}\sqrt{\kappa_{cl}} + (1 - \phi)(1 - V_{cl})\sqrt{\kappa_s} + S_w\phi\sqrt{\kappa_w} + (1 - S_w)\phi\sqrt{\kappa_a}]^2. \quad (13)$$

*Knoll and Knight* [1994] and *Knoll et al*. [1995] found under laboratory conditions that (13) fits the observed dielectric behavior of a constructed unconsolidated sand-clay mixture. As unconsolidated sand and clay are major components of near-surface systems, a dielectric mixing formula using a sand-clay model is an appropriate representation of the relation between dielectric and hydrogeologic properties for many practical applications. For this reason we also adopt a sand-clay dielectric mixing formula for our synthetic case studies.

For many hydrogeological investigations, intrinsic permeability estimates are more useful than estimates of porosity or clay fraction. *Knoll et al*. [1995] converted the relation between effective dielectric constant, saturation, porosity, and clay fraction shown in (13) to an expression between effective dielectric constant, saturation, and intrinsic permeability using petrophysical relationships. The starting point for this conversion is the expression given by *Marion et al*. [1992] for the relation between porous clay volume fraction and porosity. *Marion et al*. [1992] found using a sand-clay system under laboratory conditions that when the porous clay volume fraction ($Cl_p$) is less than that of the pure sand porosity, the clay is dispersed in the pore space of the sand and the porosity is reduced. As the porous clay volume fraction increases above the pure sand porosity, the sand grains become suspended in a clay matrix and the porosity is increased due to the microporosity of the clay. This microgeometrical porosity model can be expressed as

$$\begin{aligned} \phi &= \phi_s - Cl_p(1 - \phi_{cl}) \qquad Cl_p < \phi_s \\ \phi &= Cl_p\phi_{cl} \qquad Cl_p > \phi_s \end{aligned} \quad (14)$$

where $\phi$ is porosity and the subscripts s and cl refer to pure sand and pure clay in the sand-clay system. This model results in a cusp in the clay content versus porosity curve when the volume fraction of porous clay equals the pure sand porosity [*Marion et al*., 1992]. The relationship between porous clay volume fraction ($Cl_p$) and clay volume fraction with no microporosity ($V_{cl}$) are found through the grain densities as discussed by *Marion* [1990].

The relationship between permeability ($k$) and characteristics of the skeletal framework can be expressed in many dif-

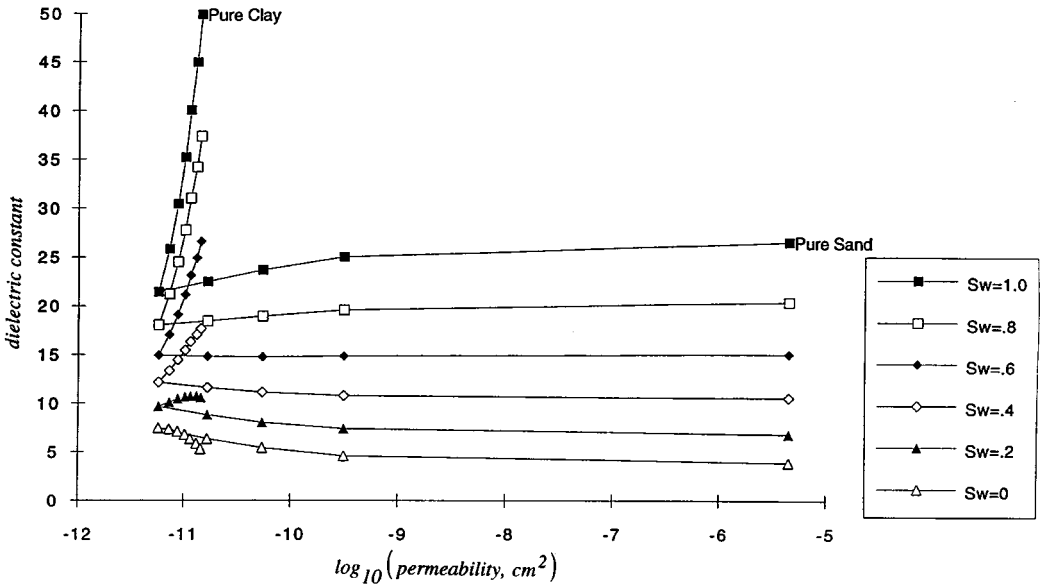


**Figure 2.** Petrophysical curves relating dielectric constant, fractional water saturation ($S_w$) and $\log_{10}$ permeability where intrinsic permeability is in square centimeters. These curves were computed using the method of *Knoll et al*. [1995]. The curves are plotted in 0.1 increments of porous clay volume fractions from pure sand (on the right) to pure clay.

ferent ways; a common formulation is given by the Kozeny-Carman relation:

$$k = \frac{\phi^3}{5(1-\phi)^2 S_s^2} \tag{15}$$

where $S_S$ is the specific surface or the surface area per solid volume. The specific surface parameter can be computed using grain size and shape following *Bear* [1972]:

$$S_s = \frac{\sum_{i=1}^{m} 4\pi r_i^2 N_i}{\sum_{i=1}^{m} 4/3\,\pi r_i^3 N_i} = 3\sum_{i=1}^{m} \frac{V_i}{r_i} \tag{16}$$

where $m$ represents the different possible size fractions, each fraction having $N_i$ spheres of radius $r_i$, and $V$ is the volume fraction of the component $i$. *Yin* [1993] substituted (16) with both sand and clay components into (15) to yield an expression for permeability:

$$k = \phi^3 \Big/ \left[ 45(1-\phi)^2 \left( \frac{V_s}{r_s} + \frac{V_{cl}}{r_{cl}} \right)^2 \right], \tag{17}$$

where $r_s$ and $r_{cl}$ are the sand and clay grain particle radii, respectively. For this study, values of $r_s = 3.75 \times 10^{-2}$ cm and $r_{cl} = 2.2 \times 10^{-5}$ cm were used in (17), and the dielectric constants of air and water were defined as $\kappa_a = 1$ and $\kappa_w = 80$ [*CRC Handbook*, 1991] and used in (13). Following the laboratory measurements made at 1 MHz by *Knoll and Knight* [1994], the pure quartz sand and pure kaolinite clay dielectric constants of $\kappa_s = 6.9$ and $\kappa_{cl} = 18$ were used in (13), and porosities of $\phi_s = 40\%$ and $\phi_{cl} = 60\%$ were used in (14). Following *Knoll et al*. [1995], (14) and (17) were used with (13) to produce the relations between dielectric constant, saturation and intrinsic permeability shown in Figure 2. These curves are plotted in increments of 10% porous clay volume fractions from the pure sand end member (on the right) to the pure clay end member. Equations (13), (14), and (17) are model petrophysical relationships that enable the transformation of dielectric information from GPR data into hydrogeological information. Although these relationships have been verified in the laboratory [*Knoll et al*., 1995], they have not been verified for use with field data at a larger scale. Additionally, at more typical field radar frequencies (e.g., 100 MHz), we would expect the sand and clay dielectric constants used in (13) to be lower [*Knoll et al*., 1995]. The curves are also not universal, as they depend on the components of the system and their associated dielectric constants; for any particular application, site-specific curves can be developed. Nonetheless, the combined relationships of (13), (14), and (17) are chosen for use in this study for the following reasons: (1) they are appropriate for a sand-clay environment, (2) they are based on microgeometrical models rather than empirical relations, and (3) they have been verified in the laboratory. The curves produced by these relationships (Figure 2) reveal that the dielectric constant is a function of both saturation and intrinsic permeability and that the dielectric constant is much more sensitive to saturation state than to the intrinsic permeability when the facies is sandy. Indeed, this insensitivity has prompted many investigators to commonly neglect the influence of permeability on the dielectric constant [*Topp et al*., 1980]. However, depending on the extent of heterogeneity of the system, information about permeability is potentially available from the dielectric constants. In this study we investigate the effectiveness of using GPR data for saturation as well as permeability estimation in three different bimodal systems, each of which are composed of two facies with different hydrogeological properties.

**Table 1.** Characteristic Values of Porous Clay Volume Fraction, Fractional Porosity, and Intrinsic Permeability for the Four Facies That Make Up the Three Systems Investigated in the Numerical Case Studies

| | Facies | | | |
|---|---|---|---|---|
| | Sand | Loamy Sand | Sandy Clay | Clay |
| Porous Clay Volume Fraction | 0.0056 | 0.10 | 0.50 | 0.80 |
| Fractional Porosity | 0.398 | 0.36 | 0.30 | 0.48 |
| Intrinsic Permeability, $cm^2$ | $10^{-7}$ | $10^{-9.51}$ | $10^{-11.14}$ | $10^{-10.94}$ |
| System I | 50% | ··· | ··· | 50% |
| System II | 50% | ··· | 50% | ··· |
| System III | 50% | 50% | ··· | ··· |

## 4. Numerical Case Studies

Numerical experiments were performed to demonstrate the effect on permeability and saturation estimates when information from GPR is included in the estimation procedure. The experiments were performed on three systems, each composed of two facies. The average hydrogeological attributes of the individual facies comprising the three systems were computed using (14) and (17) and are shown in Table 1. As shown in Table 1, the sand facies is a member of all systems; the other facies in the systems have larger clay volume fractions and are either a clay (system I), a sandy clay (system II), or a loamy sand (system III). Section 4.1 presents the construction of the "model" permeability and saturation fields from which we can compute corresponding dielectric fields. The dielectric fields represent data that are potentially available from GPR signal analysis. Section 4.2 focuses on estimation of the saturation and permeability fields using well bore data only; these estimates provide a comparison for subsequent estimation made using dielectric information. The estimation of saturation and permeability using perfect dielectric information is presented in section 4.3, and the estimation using corrupted dielectric information is discussed in section 4.4. These numerical case studies enable us to explore the potential and limitations of GPR-assisted hydrogeological parameter estimation in bimodal geological systems.

### 4.1. Construction of Synthetic Aquifers and Computation of Dielectric Fields

Construction of synthetic aquifers consisted of simulating permeability and saturation fields. In this section we create model permeability and saturation fields that we will attempt to recover using dielectric information potentially available from radar data and petrophysical relationships. Although every attempt was made to ensure that the construction of the permeability and saturation fields was realistic, this step is not part of the inversion procedure itself. Many different fields could have been created; here we investigate a geologic model that is representative of realistic field situations where characterization using GPR is feasible. For these reasons, a permeability field was simulated that represents a shallow, unconsolidated, bimodal system. The "shallow" attribute is optimal for use of surface GPR methods and is common for environmental, engineering, and agricultural sites, and "unconsolidated" is typical of near-surface material. Last, "bimodal" refers to a system composed of two facies, and thus predominantly two permeabilities, and is a simplified representation of many sedimentary depositional environments.

The parameters used for simulating the model fields were chosen based on case studies of similar aquifers from the literature. For example, the correlation length scale used for the permeability simulation is in the range reported by many authors for shallow, unconsolidated material [see review by *Gelhar*, 1993], the covariance function used to generate the model permeability field is similar to that used by *Desbarats* [1987] to model a sand-shale sequence, and the relative permeability and capillary pressure functions used for simulating the saturation fields are widely accepted in the unsaturated flow literature. Grid discretization, which is the same for the permeability, saturation and dielectric fields (Table 2), was chosen based on the expected resolution from a detailed surface GPR campaign.

Construction of the aquifers commenced with simulation of permeability fields. The structure of the permeability field was the same for systems I, II, and III, and the values assigned to the nodes varied depending on the system under consideration. The saturation fields were subsequently obtained by simulating two-dimensional water flow through the model permeability fields of each system. After construction of the synthetic aquifers, the dielectric fields were computed using the model permeability and saturation fields together with the petrophysical relationships as described in section 3.2. The details of the construction of the model permeability and saturation fields, and the computation of the corresponding dielectric fields are discussed in the following paragraphs.

**4.1.1. Construction of permeability fields.** A vertical cross section of indicator values was generated using an indicator simulator from the Geostatistical Software Library (GSLIB) group of programs [*Deutsch and Journel*, 1992]. The field consisted of two indicator values with equal selection probability which were generated with an anisotropic exponential covariance function $C(r_1, r_2)$ given by

$$C(r_1, r_2) = 0.25 \exp\left[ -\left( \frac{r_1^2}{8.5^2} + \frac{r_2^2}{0.6^2} \right)^{1/2} \right]. \quad (18)$$

In (18), 0.25 is the unconditional variance of the indicator variable, and $r_1$ and $r_2$ are the separation distances in the horizontal and vertical directions, respectively, with corresponding integral scales of 8.5 and 0.6 m. Figure 3 is a realization of this simulation and is considered the model permeability field. In this field the higher permeability, shown in light gray, represents the sand facies for all system and the lower permeability, shown in black, represents a clay facies for system I, a sandy clay for system II, and a loamy sand for system III. The facies are defined by single characteristic values of porous clay volume fraction, porosity, and intrinsic permeability as shown in Table 1. Each cell block is considered a homogeneous unit composed of one of the two facies. The facies pairs and characteristic values were chosen as a modeling decision to allow investigation of bimodal systems with different degrees of heterogeneity. In section 4.4.1 we investigate the impact of using single-characteristic values rather than ranges of parameter values to represent the facies and show that the addition of random, uncorrelated, Gaussian error to the model results in dielectric constant variations with saturation that are on the same order as those variations observed when a range of values is used to initially define the facies. For the facies and systems defined in Table 1, the petrophysical curves discussed in section 3.2 and shown in Figure 2 reduce to those shown in

**Table 2.** Grid Dimensions Used for all Permeability, Saturation and Dielectric Fields, Boundary Conditions, Initial Conditions, Fluid Properties, Relative Hydraulic Conductivity, and Relative Capillary Pressure Functions

| Parameters | Values |
|---|---|
| Grid dimensions | |
| Width | 150 m |
| Depth | 10 m |
| Discretization | 50 pixels in $x$ direction where $\Delta x = 3$ m<br>10 pixels in $z$ direction where $\Delta z = 1$ m |
| Boundary conditions | |
| No-flow boundaries | left ($x = 0$ m), right ($x = 150$ m), top ($z = 0$ m) |
| Water table | held constant at base of model |
| Initial conditions ($t = 0$) | |
| Saturation = 0.9 | ($x$, $z$): (33–39, 1), (72–78, 1), (105–111, 1) |
| Saturation = steady state conditions | all other locations |
| Fluid properties | |
| water at $T = 15$°C, $P = 1$E5 Pa | density 1000 kg/m$^3$, dynamic viscosity 1.002E-3 Pa s, compressibility 0.455E-9 1/Pa |
| Relative hydraulic conductivity* | |
| $k_{rl} = \sqrt{S^*}\,\{1 - [1 - (S^*)^{1/\lambda}]^{\lambda}\}^2$ | $\lambda = 0.457$ |
| where $S^* = \dfrac{S_l - S_{lr}}{1 - S_{lr}}$, $S_{lr} = 0.1$ | |
| Relative capillary pressure* | |
| $P_{\text{cap}} = -C([S^*]^{-1/\lambda} - 1)^{1-\lambda}$ | $C$ = strength coefficient, $\lambda = 0.457$ |
| where $S^* = \dfrac{S_l - S_{lr}}{1 - S_{lr}}$, $S_{lr} = 0.1$ | |

$S_{lr}$ is residual liquid saturation.
*From *van Genuchten* [1980].

Figures 4a–4c. These curves show that permeability and saturation values for a particular facies correspond to unique dielectric constant values and also that non-uniqueness exists when trying to map a dielectric constant into a saturation estimate when the composition of the system is unknown.

**4.1.2. Numerical simulation of saturation fields.** In this section we create model saturation fields that we will subsequently investigate using radar techniques and then try to recover using the hypothetically available radar data and petrophysical relationships. Our goal is to simulate a realistic scenario where radar data may provide some assistance in the characterization process. For each system a saturation field was computed by numerically simulating two-dimensional water flow using the TOUGH2 transport code [*Pruess*, 1991]. The grid discretization, which is the same for all components of the numerical experiments, is shown in Table 2 along with the boundary conditions, initial conditions, and fluid properties used for the numerical simulation. The input models to the numerical simulator consisted of the intrinsic permeability fields of each system whose structure is shown in Figure 3 and whose values are given in Table 1. For isothermal systems with one saturating fluid, intrinsic permeability is related to saturated hydraulic conductivity by a scalar. During simulation, these hydraulic conductivity values were modified as described by the relative hydraulic conductivity and capillary pressure functions of *van Genuchten* [1980], shown in Table 2. The strength coefficient ($C$) used in computation of the relative capillary pressure function varied for each facies and was determined using the Leverett function [*Leverett*, 1941; *Scheidegger*, 1974]. Flow was simulated through each domain for 4 years to ensure that the system was at steady state; the systems were brought to steady state to simulate natural field conditions in the absence of any external flux. After steady state was reached, instantaneous sources were imposed at three surface locations to simulate localized infiltration due to, for example, a spill of fluid with similar properties as water. Initial conditions of 90% water saturation at time zero were imposed at the locations given in Table 2 to simulate the infiltration, and these plumes were then allowed to migrate under combined gravity and capillary forces. We are interested in investigating the saturation fields at a time after introduction of the infiltration events that is sufficient for coordinating a GPR survey at the site and is also large enough to have allowed some migration of the plumes. We chose to investigate the saturation fields after two months of infiltration; Plates 1a–1c show snapshots of the resulting saturation fields at this time. The fields of Plates 1a–1c are considered to be the saturation fields at the time of the GPR survey and are referred to as the model saturation fields for the three systems under consideration.

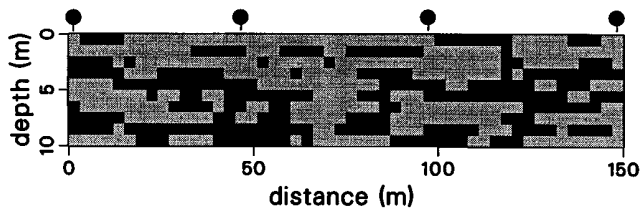


**Figure 3.** Model intrinsic permeability field cross section representing a system composed of a sand facies (light gray) and another facies (black) as described in text. The locations of four boreholes from which borehole data were considered available are shown above the cross section.

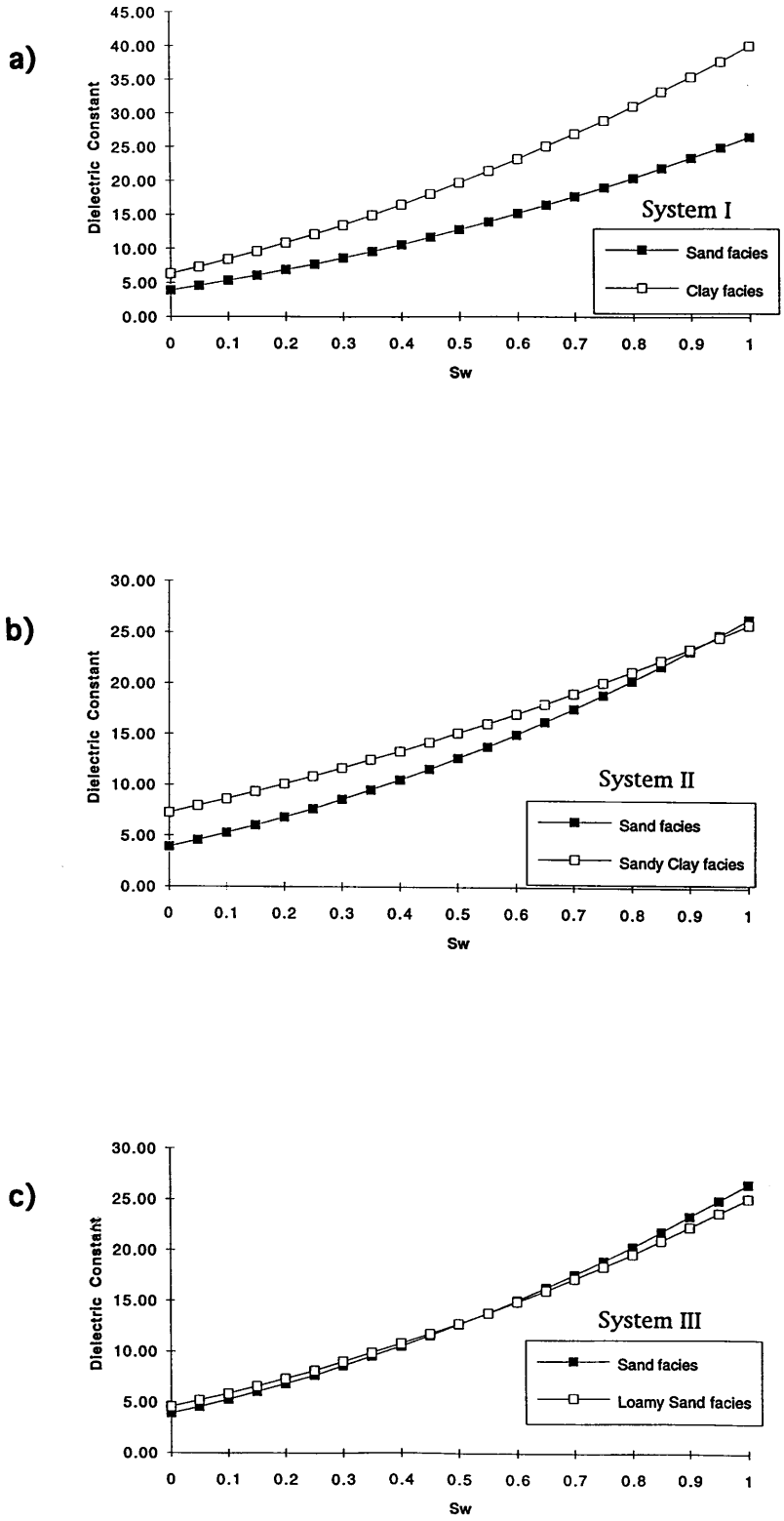


**Figure 4.** Petrophysical curves relating dielectric constants and fractional water saturation ($S_w$) for (a) system I, (b) system II, and (c) system III (refer to Table 1 for facies descriptions).

**4.1.3. Computation of dielectric fields.** The dielectric fields were computed using the model permeability and saturation fields of each system together with the dual-facies petrophysical curves shown in Figures 4a–4c. The dielectric fields, shown in Plates 2a–2c represent data potentially available from GPR if signal penetration is sufficient and data collection and inversion into dielectric constants were perfect. The grid dimensions used for the dielectric fields are the same as those

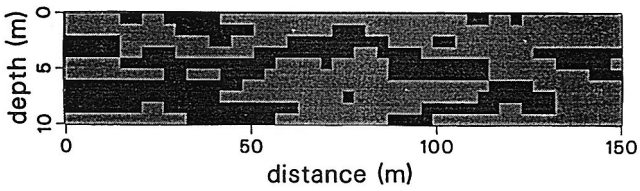


**Figure 5.** Intrinsic permeability field realization obtained from sequential indicator simulation conditioned on the available borehole data. Light gray represents the sand facies and black represents the other facies in the system under consideration (refer to Table 1).

given in Table 2, and thus for the computation of these dielectric fields we assume that velocity estimations were obtainable from the GPR data every 1 m vertically and 3 m laterally. Evenly spaced velocity estimates, for example, from cross-hole inversion, can be used directly with (12) to obtain dielectric estimates. If estimation of the velocities from surface GPR are not uniformly spaced, interpolation of the velocity field at the desired grid dimensions is necessary prior to conversion of the velocities to dielectric estimates using (12). The ability to estimate velocities in the vertical direction is a function of the vertical resolution, which depends on the radar frequency. For a constant center frequency of 100 MHz, GPR wavelengths for the pure sand end member ($\kappa_s = 6.9$) and the pure clay end member ($\kappa_{cl} = 18$) used in (13) are 1.14 and 0.71 m, respectively. As reflections that can be used for velocity analysis are usually considered to be distinguishable at a minimum spacing of a quarter of a wavelength, the assumption of obtaining velocity estimates at the 1-m vertical grid spacing of this model is not unreasonable.

### 4.2. Saturation and Permeability Estimation Using Only Limited Well Bore Data

We turn now to the process of estimating permeability and saturation fields. Our goal is to recover the model permeability and saturation fields that were created in sections 4.1.1 and 4.1.2, respectively. For the estimation process we have available a field of dielectric values, petrophysical relationships between dielectric values and hydraulic parameters, and limited well bore data. From the well bore data it is assumed that we have determined that the system can be categorized into two facies and that we know the average hydrological properties of the facies as described in Table 1. In this section we estimate the hydraulic parameters using only the limited well bore data. The estimates obtained here (1) provide a comparison with the hydraulic estimates obtained using GPR-assisted techniques that will be described in the next section and (2) provide input that is required for the GPR-assisted estimation procedure.

**4.2.1. Permeability estimation.** In this example, 40 intrinsic permeability measurements were considered available from the four boreholes whose locations are shown in Figure 3. The samples are considered to be collected every meter vertically, or one sample per cell block. Since each cell block is homogeneous, the measured samples within the cell block are considered to have the same properties as the entire $3 \times 1$ m cell block. For a field investigation, well bore hydraulic conductivity measurements could be obtained using a variety of methods, as discussed in section 1, and then scaled to intrinsic permeability values. The scale of the measurement and thus its relationship to the volume of the cell block will vary depending on the measurement technique, and in a field investigation it is likely that some adjustment will be necessary to match the measurement and modeling scales. The issues of scale in hydrologic modeling are complex and are beyond the scope of this discussion; the reader is referred to work by *Kalma and Sivapalan* [1995], *Sanchez-Vila et al.* [1995], and *Rubin and Gomez-Hernandez* [1990].

For the permeability estimation using only well bore data, the well bore permeability values were transformed into indicator variables and sequential indicator simulation from the GSLIB group of programs [*Deutsch and Journel*, 1992] was performed. This process [*Gomez-Hernandez and Srivastava*, 1990] estimates the probability that the node is in a particular category by indicator kriging conditional to measurements and previously simulated nodes values. The probability can be estimated by the conditional indicator expectation [*Gomez-Hernandez and Srivastava*, 1990]:

$$\langle I^c(\underline{x})\rangle = \text{prob}\,(I(\underline{x}) = 1), \tag{19}$$

which varies between 0 and 1 and where, for this problem, $x = (x_1, x_2)$. After computation of the probability at a node, a random variable $U$ is drawn from a uniform distribution (0, 1). If $U > \langle I^c(\underline{x})\rangle$, the value of the node is assigned the indicator value of 1; otherwise, it is assigned the value of 0. The newly simulated value at that node is included in the conditioning

**Table 3.** Percent of Correct Intrinsic Permeability Values of the Estimated Fields Compared to the Model Intrinsic Permeability Fields

| Data | | System I* | System II† | System III‡ |
|---|---|---|---|---|
| Well bore data only | estimated by indicator simulation | 65 | 65 | 65 |
| Well bore data with perfect dielectric field | $\langle S\rangle$ from fluid modeling | 98 | 84 | 69 |
| | $\langle S\rangle^c$ from kriging saturation measurements | 93 | 81 | 67 |
| Well bore data with corrupted dielectric field | spatially uncorrelated error with coefficient of variation = 0.2, $\langle S\rangle$ from fluid modeling | 93 | 76 | 58 |
| | spatially uncorrelated error with coefficient of variation = 0.4, $\langle S\rangle$ from fluid modeling | 83 | 64 | 49 |
| | systematic error, $\langle S\rangle$ from fluid modeling | 92 | 77 | 56 |

Results are shown for three different systems and for six different cases which are distinguished by the data available for estimation. All values are in percent.

*Fifty percent sand, 50% clay.

†Fifty percent sand, 50% sandy clay.

‡Fifty percent sand, 50% loamy sand.

**Table 4.** Correlation Coefficients Between the Estimated and Model Saturation Fields

| Data | | System I* | System II† | System III‡ |
|---|---|---|---|---|
| Well bore data only | estimated by fluid modeling | 0.640 | 0.620 | 0.743 |
| | estimated by kriging saturation measurements | 0.652 | 0.678 | 0.770 |
| Well bore data with perfect dielectric field | $\langle S \rangle$ from fluid modeling | 0.996 | 0.998 | 0.999 |
| | $\langle S \rangle^c$ from kriging saturation measurements | 0.978 | 0.992 | 0.999 |
| Well bore data with corrupted dielectric field | spatially uncorrelated error with coefficient of variation = 0.2, $\langle S \rangle$ from fluid modeling | 0.935 | 0.894 | 0.943 |
| | spatially uncorrelated error with coefficient of variation = 0.4, $\langle S \rangle$ from fluid modeling | 0.777 | 0.751 | 0.800 |
| | systematic error, $\langle S \rangle$ from fluid modeling | 0.948 | 0.919 | 0.951 |

Results are shown for three different systems and for seven different cases which are distinguished by the data available for estimation.
*Fifty percent sand, 50% clay.
†Fifty percent sand, 50% sandy clay.
‡Fifty percent sand, 50% loamy sand.

indicator data set and the process proceeds sequentially until all nodes have been simulated. For our problem the sequential indicator simulation was performed conditional to the borehole measurements using the same covariance function (18) that was used to simulate the data. In a real field investigation, a covariance function could be estimated by considering a combination of variogram analysis of the borehole data and knowledge of covariance functions from similar geological environments such as those tabulated by *Gelhar* [1993]. After simulation of the entire field, the indicator values were transferred back into permeability values. The simulated permeability field is shown in Figure 5 where the light gray represents the sand facies and the black represents the other facies in the system (refer to Table 1). A node-by-node comparison of the permeability fields simulated using the borehole data with the model permeability fields reveals that the permeabilities were predicted correctly 65% of the time, as shown in Table 3; this percentage was typical of those found for all realizations. In a real field investigation, given the lack of available information on the horizontal correlation structure, the true covariance function would be unknown and thus Figure 5 is among the best simulations of a permeability field possible when using only borehole data.

**4.2.2. Saturation estimation.** In this section we focus on estimating the saturation fields using only well bore data. The saturation field can be estimated in different ways. In this study, numerical flow simulation and kriging techniques were used to obtain estimates of the saturation fields using well bore permeability and saturation measurements, respectively. The estimation of this saturation field serves two purposes: it provides a comparison between estimates obtained using borehole data only and those obtained using information from GPR data, and it also produces the estimates of $\langle S \rangle$ and $\langle S \rangle^c$ in (9) or (10), respectively, which are required for the GPR-assisted saturation estimation. We chose to present two methods of saturation estimation using well bore data to show the similarities in estimation using the different techniques as well as to provide examples of different techniques that can be used to compute the expected saturation fields needed for the GPR-assisted saturation estimation procedure.

To obtain an unconditional estimate of the saturation field at the time of the GPR survey, numerical flow simulation was performed using the same grid dimensions, boundary conditions, fluid properties, and relative hydraulic conductivity and capillary pressure functions shown in Table 2. The input intrinsic permeability model (which is scaled to saturated hydraulic conductivity model within the flow simulation) consisted of a homogeneous domain whose value was obtained by taking the geometric mean of the sampled well bore intrinsic permeabilities. The geometric mean of the sampled values was used as input instead of the permeability estimates based on the indicator simulation using the borehole data (Figure 5) because, as previously stated, the indicator simulation is likely to be a better estimate than what is realistically obtainable from the sampled permeabilities. Additionally, as the computed estimate serves as an input to the GPR-assisted estimation technique, we desired to keep the procedure simple. Initial conditions consisted of linear gradients from 10% saturation at the ground surface to full saturation at the water table. The exact locations of the localized infiltration events were not considered to be known, as they are not penetrated by the well bores and thus they were not included as initial conditions in the flow simulation. Flow was simulated using the fluid properties, relative hydraulic conductivity function and relative capillary pressure function shown in Table 2 for approximately the same time as the known time interval between the infiltration event and the time of the GPR survey, or for approximately 2 months. The resulting field is shown in Plate 3a and represents a simple estimate of what could be interpreted as the saturation field if only sparse wellbore permeability data were available. The correlation coefficient between this expected saturation field and the model saturation field for system I is 0.64; this correlation can be increased by conditioning the estimated field on well bore saturation measurements, if they are available, or by using a nonstationary permeability field computed with the borehole data as discussed earlier. The results of the saturation estimation for the other systems using the same technique are shown in Table 4. This table shows that the best correlation between the estimated saturation field and the model saturation field is found for system III, where the permeability values of the facies that comprise the system are most similar.

The conditional saturation estimate was obtained using the method of ordinary kriging of the wellbore saturation measurements. These estimates are obtainable using the techniques discussed in section 1 and are considered to be available from the model saturation fields at the borehole locations shown in Figure 3. Ordinary kriging is based on the principles of geostatistics whereby an estimate of $\hat{Z}$ at an unsampled

location ($\underline{x}$) is given as the linear sum of the $N$ known values by

$$\hat{Z}(\underline{x}) = \sum_{i=1}^{N} \lambda_i Z(x_i) \tag{20}$$

where $\lambda_i$ ($i = 1, \cdots, N$) are the kriging weights that are obtained by requiring (1) that all weights lie between 0 and 1 and sum to 1, (2) that the estimation error associated with $\hat{Z}(\underline{x})$ is minimal, and (3) that the expected error is zero or, equivalently, that the estimate is unbiased. These criteria translate into a system of linear algebraic equations which are solved to obtain $\lambda_i$ for each of the unsampled sites [*Delhomme*, 1978]. A key component of this system of algebraic equations is the spatial covariance of the attribute $Z(x)$ which weighs the contributions from various measurements according to their relative distance from $\underline{x}$. For system I the anisotropic exponential covariance function $C(r_1, r_2)$ used in the ordinary kriging procedure to estimate the saturation field is given by

$$C(r_1, r_2) = 0.123 \exp\left[-\left(\frac{r_1^2}{23^2} + \frac{r_2^2}{1.2^2}\right)^{1/2}\right] \tag{21}$$

where 0.123 is the variance of the well bore saturation measurements, and $r_1$ and $r_2$ are the separation distances in the horizontal and vertical directions, respectively, with corresponding integral scales of 23 m and 1.2 m, respectively. This function was based on experimental variogram analysis of saturation measurements taken from the saturation field shown in Plate 1a at the borehole locations shown in Figure 3. Although there is a dearth of information on the horizontal correlation structure, the horizontal integral scale used in (21) is in line with others estimated using variogram analysis of densely sampled water content measurements collected in unconsolidated, heterogeneous media [*Rubin et al.*, 1992b]. The estimated saturation field found from kriging the well bore saturation measurements using (20) and (21) is shown in Plate 3b. The correlation coefficient between this expected field and the model saturation field for system I (Plate 1a) is 0.652. Similar analyses were performed for each system, and the correlation coefficients between the estimated and model saturation fields are shown in Table 4. Again, the best estimates of the saturation field are those of system III, where the permeability of the facies that comprise the system are most similar.

The estimation of saturation using well bore data only has been attempted here using numerical flow simulation and kriging techniques. For all systems the correlation coefficient between the estimated and model saturation fields lie between 0.6–0.8 and the differences between the estimates obtained using numerical flow simulation and those obtained using kriging techniques were minor. Again we stress that other estimation procedures are possible and that the estimated saturation values and associated correlation coefficients will vary depend-

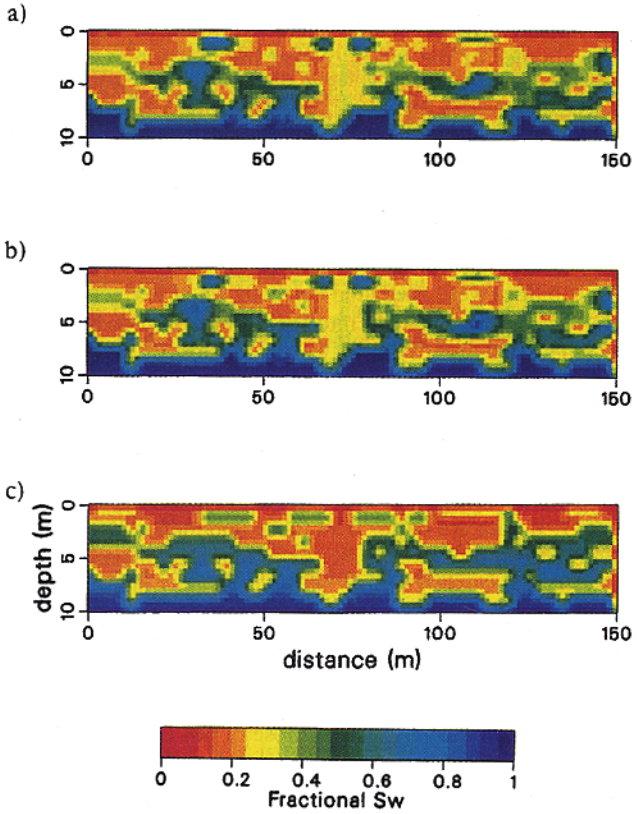


**Plate 1.** Model saturation fields created by simulating water flow through the permeability fields whose structure is shown in Figure 3 and whose values are given in Table 1: (a) system I, (b) system II, and (c) system III. The top of the vertical cross section represents the ground surface and the water table was held constant at the bottom of the figure. $S_w$ is water saturation.

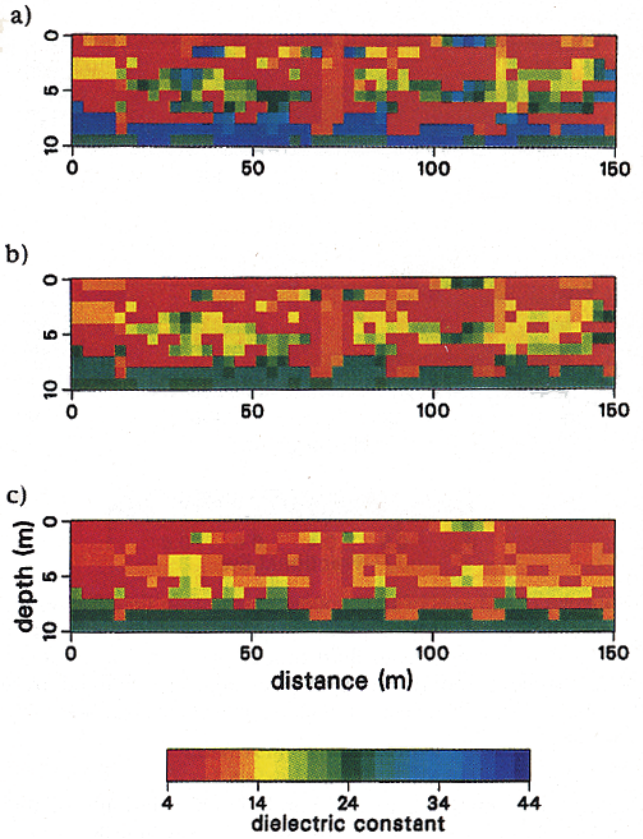


**Plate 2.** Dielectric field cross sections computed using the model intrinsic permeability and saturation fields with the dual-facies petrophysical curves shown in Figures 4a–4c for (a) system I, (b) system II, and (c) system III. These dielectric fields can potentially be obtained from analysis of CMP or cross-hole GPR data in an ideal bimodal system.

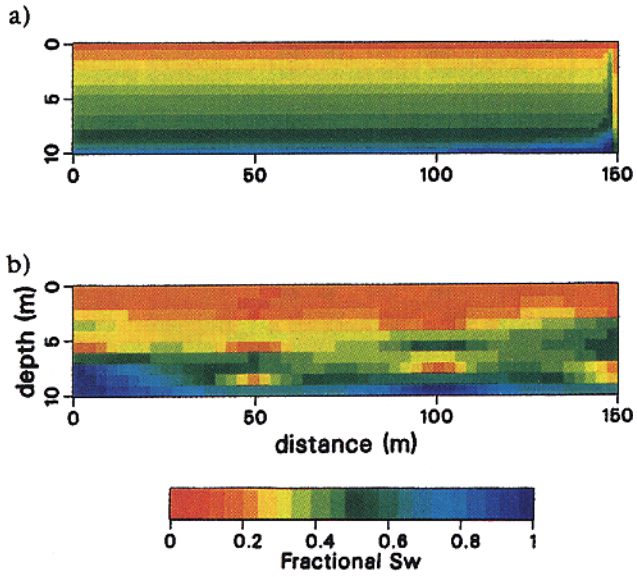


**Plate 3.** Estimates of the expected saturation field for system I obtained using only limited borehole data: (a) saturation estimation obtained from fluid modeling through a homogeneous domain and (b) saturation estimation obtained from kriging saturation measurements. $S_w$ is water saturation.

ing on the technique used and borehole information availability. We chose the methods presented here primarily to keep the GPR-assisted technique, which uses these estimates, procedurally simple. In sections 4.3 and 4.4 the estimates obtained here are incorporated with information from GPR data into the estimation procedure.

### 4.3. Saturation and Permeability Estimation Using Perfect Dielectric Information

We now strive to improve the estimates of saturation and permeability over those found in section 4.2 by incorporating information potentially obtainable from radar data. We assume that some borehole information, a perfect and complete field of dielectric constants, and petrophysical relations are available for the inversion. We also assume, given the high-resolution nature of GPR data, that information from GPR can be used jointly with appropriately scaled well bore measurements. For the bimodal systems under consideration, (1)–(11) form the basis of this GPR-assisted hydraulic estimation procedure.

**4.3.1. Saturation estimation.** The probability of realizing a saturation value of $S_1$ can be calculated using (9) or (10) with $\langle S \rangle$ or $\langle S \rangle^c$ described in section 4.2.2 and the values of $S_1$ and $S_2$ inferred from the dielectric constants of the corresponding system and the petrophysical relations for bimodal systems. The ML estimate of saturation at each pixel is that value ($S_1(\underline{x})$ or $S_2(\underline{x})$) that maximizes the likelihood function (11). In the case of a binary permeability field with equal selection probability, a $P_S$ or $P_S^c$ value greater than 0.5 occurs when the expected saturation value is closer to $S_1$, and thus $S_1(\underline{x})$ is retained at that location as the estimated saturation value. Similarly, if the calculated $P_S$ or $P_S^c$ value is less than 0.5, $S_2(\underline{x})$ is chosen as the estimated saturation value. For example, for system I a dielectric constant of 15 at a particular location yields the saturation options of $S_1 = 0.36$ and $S_2 = 0.60$ (Figure 4a). If the value of $\langle S \rangle$ at that location is 0.52, then $P_S$ calculated using (9) is 0.33. Since $P_S < 0.5$, the value of $S_2$ of 0.60 is retained at that location as the saturation estimate.

The saturation fields estimated in this manner for system I using both $\langle S \rangle$ from fluid flow simulation and $\langle S \rangle^c$ from kriging of wellbore saturation measurements are shown in Plates 4a and 4b, respectively. Both of these estimated fields bear a remarkable similarity to the model saturation field for system I shown in Plate 1a. Indeed, node-by-node comparisons reveal that the correlation coefficients between the estimated and model fields for system I are 0.996 and 0.978 (Table 4). Results from comparing saturation estimations obtained using perfect information from GPR data with the model saturation fields for systems II and III are also shown in Table 4. These results indicate that (1) under all circumstances, the correlation coefficient between the estimated fields and the model fields is greater than 0.95, (2) under all circumstances, the correlation coefficients for the cases where dielectric information is included in the estimation process are higher than those obtained from borehole information alone, and (3) the best saturation estimates were obtained when investigating system III, where the permeabilities of the two facies comprising the system are most similar. This result is reasonable upon examination of the petrophysical curves for system III (Figure 4c), which show that regardless of the facies at a particular location, the dielectric constant will yield a reasonable saturation estimate.

**4.3.2. Permeability estimation.** For a given value of dielectric constant, there is a one-to-one relation between $S_1$ and $k_1$ and, similarly, between $S_2$ and $k_2$, where $k_1$ and $k_2$ are permeabilities of the facies comprising the system. Thus the probability of observing $k_1$ is the same as the probability of observing $S_1$, and we are justified in using the probability values obtained in section 4.3.1 to estimate the permeability field. The estimated intrinsic permeability fields for system I obtained from maximizing the likelihood functions (7) are shown in Figures 6a and 6b. Comparison of this estimated field with the model field for system I (Figure 3) reveals that the permeabilities were predicted correctly when perfect information from GPR is included into the estimation process 98% of the time when the $\langle S \rangle$ used for calculation of was obtained from fluid modeling and 93% of the time when $\langle S \rangle^c$ was obtained from kriging well bore saturation measurements. The results for the permeability estimations of systems II and III are shown in Table 3, and suggest that (1) under all circumstance, the estimations obtained using perfect information from GPR data are better than those obtained using well bore data alone, and (2) the ability to estimate permeability using radar data decreases as the system becomes more homogeneous, or the petrophysical curves of the system become more similar (Figures 4a–4c). The intrinsic permeability estimated using radar data can be scaled to saturated hydraulic conductivity and used with the estimates of the saturation field and functional relationships such as those of *van Genuchten* [1980] to estimate unsaturated hydraulic conductivities.

### 4.4. Saturation and Permeability Estimation Using Corrupted Dielectric Field

In the preceding example it was assumed that the interval velocities were known completely and exactly and thus the dielectric constants could be precisely determined at all locations. Given the petrophysical relations and a bimodel system, an ML estimation technique was used to estimate permeability

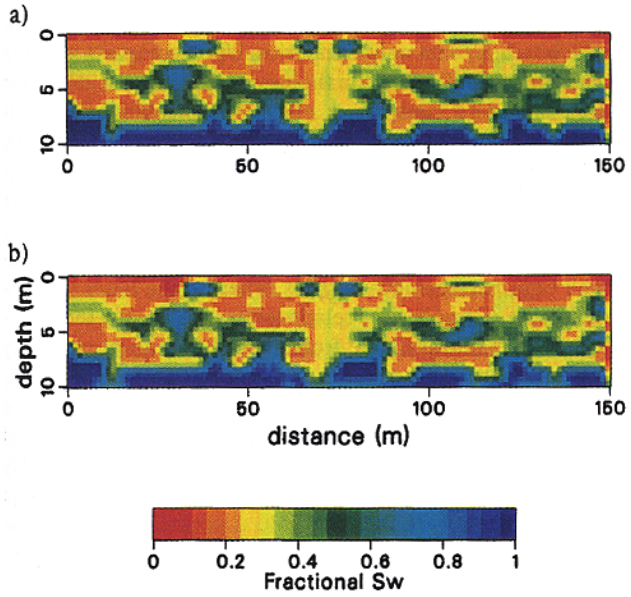


**Plate 4.** Saturated field of system I estimated using a perfect dielectric field where (a) $\langle S \rangle$ was obtained from fluid modeling through a homogeneous domain, and (b) $\langle S \rangle^c$ was obtained from kriging well bore saturation measurements. $S_w$ is water saturation.

and saturation from the error-free dielectric fields. In reality, there are errors associated with assumptions about the bimodality of the geologic system and subsequent representation of the facies using single characteristic values as shown in Table 1, as well as errors associated with GPR data collection and processing, the petrophysical model, the transfer of velocities to dielectric constants using (12). To account for these errors, we add (1) spatially uncorrelated Gaussian error, and, alternatively, (2) systematic Gaussian error to the dielectric constant fields shown in Plates 2a–2c. The corrupted dielectric fields are then considered the data available for the GPR-assisted hydraulic parameter estimation procedure and estimates of saturation and permeability are obtained following the methodology presented in 4.3. Neither approach of adding error to the data is indicative of error associated with a particular acquisition system, geometry, inversion routine, petrophysical model, or geological system. However, by considering both spatially correlated and systematic error, we attempt to show that the proposed procedure is robust enough to assist in the estimation of hydraulic parameters under a variety of circumstances.

**4.4.1. Hydraulic parameter estimation using dielectric fields corrupted with spatially uncorrelated Gaussian error.** The large number of contributing factors to the error field as discussed above suggests that, on the basis of the central limit theorem, the error field is Gaussian. This argument is in line with that presented by *Carrera and Neuman* [1986] regarding the errors distribution associated with hydraulic head estimates. To estimate the influence of velocity analysis errors on the dielectric constant estimate, the variance interval velocity error ($\sigma_V^2$) is first related to the variance of the dielectric constant ($\sigma_\kappa^2$) using a first-order error propagation method:

$$\sigma_\kappa^2 = \left(\frac{d\kappa}{dV}\right)^2 \sigma_V^2 \tag{22}$$

where the change in dielectric constant with interval velocity can be obtained by differentiation of (12). *Tillard and Dubois* [1995] compared velocity analysis of surface GPR data with a velocity profile obtained from laboratory core measurements of dielectric permitivity at the same site. They found that interval velocity errors due to uncertainties in reflection time picking, velocity analysis procedures, and the magnification of these errors using the Dix interval velocity computation of up to 10% were not uncommon. Error due to velocity analysis is assumed to be normally distributed, and 95% of this error is assumed to fall within 10% of the true value of velocity at a given location ($\underline{x}$), which can be expressed as

$$2\sigma_V(\underline{x}) = 0.1V(\underline{x}). \tag{23}$$

Using relations from (12) and (22) in (23) results in a relationship between the standard deviation of the dielectric constant due to the velocity error and the dielectric constant itself at a particular location:

$$\sigma_\kappa(\underline{x}) = 0.1\kappa(\underline{x}), \tag{24}$$

or a coefficient of variation of 0.1. To account for an error due to velocity estimation of up to 10% of the actual values as well as error from the other potential contributors, for simplicity's sake we place all of the error in the dielectric data and assume that the errors are Gaussian. To simulate these compound errors, spatially uncorrelated, random Gaussian error was added to the original dielectric fields two different times, once with coefficient of variation of 0.2 and once with a coefficient of variation of 0.4. As the added errors are a function of the values at each location, the higher dielectric constant values have, on average, higher errors. This is justified, as higher values of dielectric constants are associated with high saturation or high clay content, where GPR acquisition is generally more difficult. Assuming that the two different corrupted dielectric fields are obtained from the analysis of surface or cross-hole GPR data analysis, we estimated the saturation and permeability fields using the dielectric data fields and $\langle S \rangle$ from numerical flow simulation (as calculated in section 4.2.2) in the

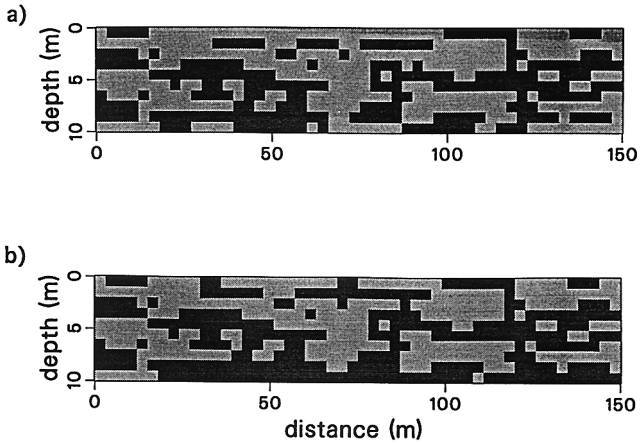


**Figure 6.** Intrinsic permeability field of system I estimated using a perfect dielectric field where (a) $\langle S \rangle$ was obtained from fluid modeling through a homogeneous domain and (b) $\langle S \rangle^c$ was obtained from kriging well bore saturation measurements. Light gray represents the sand facies and black represents the clay facies.

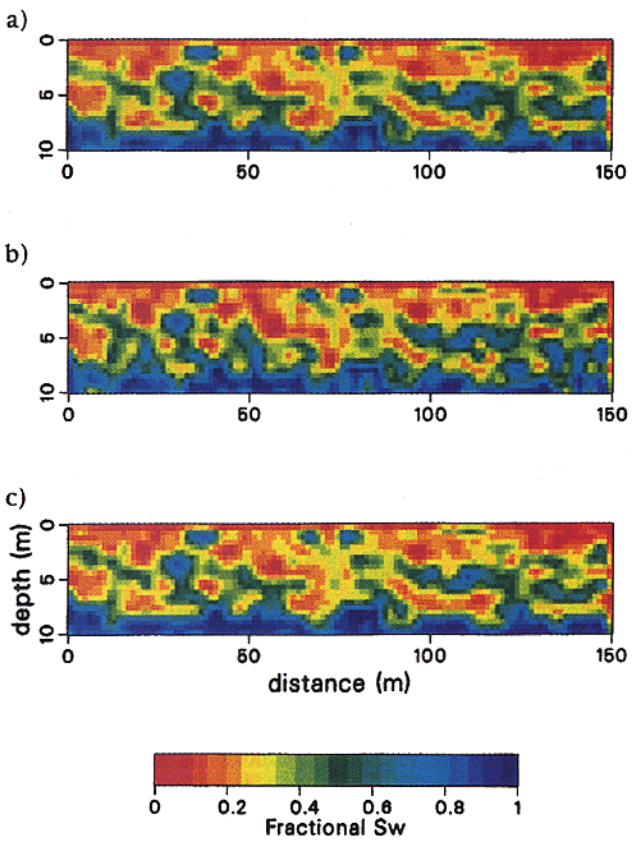


**Plate 5.** Saturation field of system I estimated using a dielectric field corrupted by (a) spatially uncorrelated Gaussian error with a coefficient of variation of 0.20, (b) spatially uncorrelated Gaussian error with a coefficient of variation of 0.40, and (c) spatially correlated Gaussian error. In all cases $\langle S \rangle$ was computed by fluid modeling. $S_w$ is water saturation.

ML procedure described in sections 4.3.1 and 4.3.2, respectively.

The estimated saturation fields for system I that were computed using dielectric fields corrupted with Gaussian noise having coefficient of variation of 0.2 and 0.4 are shown in Plates 5a and 5b, respectively. The correlation coefficient between the model and estimated saturation field for the case of the 0.2 coefficient of variation is 0.935, and for the case of 0.4 error coefficient of variation it is 0.777. The corresponding estimated permeability fields for system I are shown in Figures 7a and 7b. These permeability values were estimated correctly 93% of the time when the error coefficient of variation was 0.20 and 83% of the time when the error coefficient of variation was 0.40. The results for GPR-assisted estimation of permeability and saturation using corrupted dielectric fields for the other systems are shown in Tables 3 and 4, respectively. In comparing the estimated and model saturation fields, Table 4 shows that under all circumstances, the saturation estimates are worse than those estimates predicted when the data were error-free but are still better than those predicted using well bore data alone. Table 3 shows that the permeability estimate is best when the petrophysical curves shown in Figures 4a–4c are distinct, as are the curves for system I. However, as error increases and as the curves become more similar to those in system III (Figure 4c) or, equivalently, the system becomes more homogeneous, the GPR-assisted procedure is not able to distinguish between the facies and permeability estimation using the borehole data only is superior. Upon comparison of the results shown in Table 4 for the cases of corrupted data, two factors should be considered: (1) the permeability field estimated using only well bore data is the best estimation possible, as discussed in 4.2.1, and (2) the permeability estimation procedure using only well bore data is independent from the permeability estimation procedure using corrupted dielectric information. The former was obtained by indicator simulation of well bore permeability samples, whereas the latter was obtained using petrophysical relationships to transfer the information potentially available from GPR data into permeability estimates. Although not pursued here, the permeability estimates obtained using dielectric information can be improved by considering the estimated field to be a "prior" estimate and then conditioning this field on the local borehole permeability measurements. *Copty et al.* [1993] showed that when corrupted geophysical data were included into a permeability inversion procedure using Bayesian updating regardless of the magnitude of the error in the geophysical data, the resulting estimations were better than, or in the worse case, equal to, the estimation obtained using hydrogeological data only.

To investigate the error contribution resulting from representing a facies using a single characteristic value of porous clay volume fraction rather than a range of clay content values, we compare the variations in dielectric constants of single-valued facies that have been corrupted by the addition of spatially uncorrelated Gaussian error with a coefficient of variation of 0.20 to dielectric constant variations of facies defined

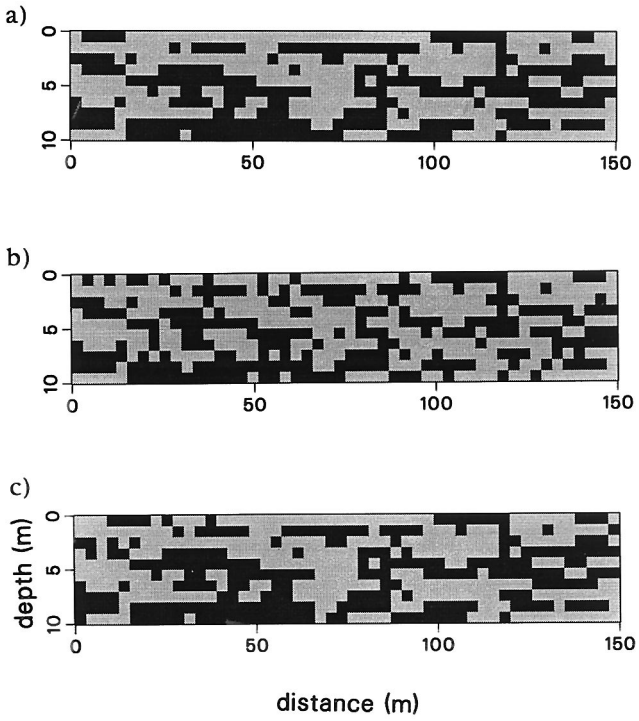


**Figure 7.** Intrinsic permeability field of system I estimated using a dielectric field corrupted by (a) spatially uncorrelated Gaussian error with a coefficient of variation of 0.20, (b) spatially uncorrelated Gaussian error with a coefficient of variation of 0.40, and (c) spatially correlated Gaussian error. Light gray represents the sand facies and black represents the clay facies.

using a clay content range. The dark line in Figure 8a represents the dielectric constant versus saturation values for sandy clay facies with a characteristic porous clay volume fraction of 0.5; this curve is the same as the sandy clay facies curve shown in Figure 4b. The upper and lower smooth, dashed lines represent the values for lithologies with porous clay content values of 60% and 40%, respectively. The jagged dotted line represents characteristic value dielectric constants that have been corrupted with spatially uncorrelated, Gaussian error having a coefficient of variation of 0.2. Figure 8b shows similar curves for the sandy facies (which has a characteristic porous clay volume fraction of 0.0056), where the values associated with the sandy facies are shown by the dark line, the dashed line represents values for lithologies composed of 20% clay, and the jagged dotted line represents characteristic value dielectric constants for the sandy facies that have been corrupted with spatially uncorrelated, Gaussian error having a coefficient of variation of 0.2. Figures 8a and 8b reveal that the dielectric constants of the low permeability facies vary more as a function of clay volume fraction range than do the dielectric constants of the high permeability facies, which is also apparent on the saturated curve shown in Figure 2. Figure 8a suggests that the variations in dielectric constants resulting from considering a 20% clay content range is similar to the variations caused by adding Gaussian error with a correlation of coefficient of 0.20 to the single-valued model. Therefore the results of the numerical simulation where error with a 0.40 coefficient of variation has been added to the system is probably representative of the estimation results one might expect to obtain in a low permeability system if additional factors also contribute to the error. However, in sandy systems, where GPR performance is optimal, the variations in dielectric constant introduced by representing the facies with a range of values rather than with a single characteristic clay content value is on average less than the variations caused by adding Gaussian error with a coefficient of variation of 0.2 to the single-valued model. This suggests that the results of the numerical simulation where error with a 0.20 coefficient of variation has been added to the system are representative of the estimation results that one might expect in a high permeability system.

**4.4.2. Hydraulic parameter estimation using dielectric fields corrupted with systematic Gaussian error.** Under some circumstances, errors stemming from certain components of the inversion procedure may dominate the error field. For example, as discussed in section 3.1 and shown in Figure 1b, the resolution in velocity analysis may increase with depth or, equivalently, there may be less error in the velocity estimates with depth. To simulate this increasing confidence in the velocity estimates with depth, Gaussian error with a coefficient of variation that varied systematically as a function of depth was added to the dielectric fields. For the depths between 0 and 2 m below the ground surface, the coefficient of variation was the highest (0.3); for depths between 2 and 4 m the coefficient of variation was 0.25; for depths between 4 and 6 m the coefficient of variation was 0.2; for depths between 6 and 8 m the coefficient of variation was 0.15; and for depths between 8 and 10 m the coefficient of variation was the lowest, 0.1. By adding systematic error to the data, we are not implying that this is the anticipated error field for any particular circumstance; rather, we are investigating the performance of the GPR-assisted estimation procedure when spatially correlated error exists. Again, the added error is a function of the dielec-

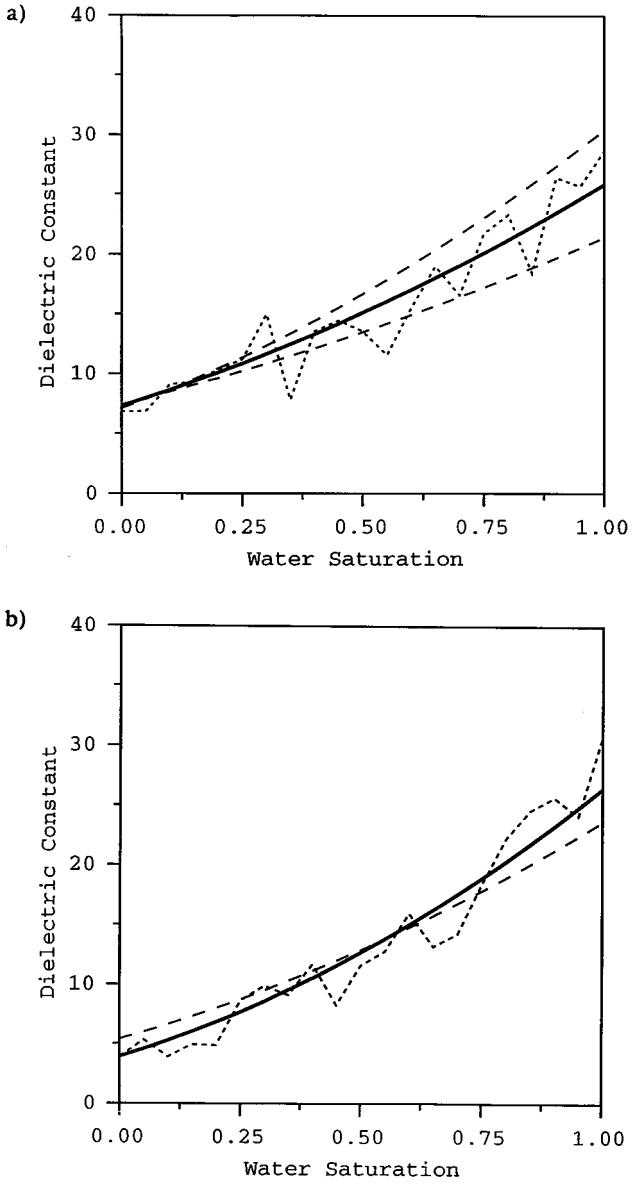


**Figure 8.** Comparison of variations dielectric constants associated with a facies defined by a 0.20 clay content range with variations caused by the addition of spatially uncorrelated, Gaussian error with a coefficient of variation of 0.20 to the single-valued facies described in Table 1. (a) Dark line represents dielectric constants versus saturation values for the sandy clay facies with a characteristic clay content value of 0.5. Upper and lower dashed smooth lines represent values associated with lithologies having 0.6 and 0.4 porous clay volume fractions, respectively. The jagged dotted line represents characteristic value dielectric constants that have been corrupted with Gaussian error having a coefficient of variation of 0.20. (b) Dark line represents the dielectric constants versus saturation for the sandy facies having a characteristic clay content value of 0.0056, and the dashed smooth line represents those values associated with a 0.2 porous clay volume fraction material. The jagged dotted line represents characteristic value dielectric constants that have been corrupted with Gaussian error having a coefficient of variation of 0.2.

tric measurement and thus areas of high saturation or clay content will be, on average, associated with higher errors.

Assuming that the dielectric fields with the systematic error are data obtained from surface CMP or cross-hole tomographic GPR analysis, we estimated the saturation and permeability fields as before using corrupted dielectric data in the ML procedure described in sections 4.3.1 and 4.3.2, respectively, where $\langle S \rangle$ was estimated by fluid flow simulation. The estimated saturation and permeability fields for system I are shown in Plate 5c and Figure 7c, respectively. For this system the correlation coefficient between the model and estimated saturation field is 0.948 and the permeabilities were estimated correctly 92% of the time. The results of the permeability estimations for all systems corrupted with systematic error are shown in Table 3. As with the case of the dielectric field with spatially uncorrelated Gaussian error, the GPR-assisted permeability estimates are improved over those obtained using well bore data alone when the system is highly heterogeneous (systems I and II), but the procedure performs poorly when the facies that comprise the system are similar, as in system III. As discussed in 4.4.1, these estimates can be improved by conditioning on available borehole permeability measurements. Table 4 shows the correlation coefficients between the model and the saturation fields estimated using a dielectric field corrupted with systematic error. In all cases the saturation estimates using a corrupted dielectric field are superior to those estimates obtained using borehole data alone and the best estimates are obtained when the system is most homogeneous (system III; Figure 4c).

## 5. Conclusions

A new technique is presented to estimate saturation and intrinsic permeability in the vadose zone. This technique incorporates information from GPR data and petrophysical relationships in the hydraulic parameter estimation procedure. The GPR-assisted estimation procedure consists of several steps. We cast the estimation problem in a stochastic framework by investigating ideal systems composed of two facies where permeability values are defined as binary random variables. The intrinsic permeability values used in this study are representative of shallow, unconsolidated systems; other systems can also be investigated where warranted. This GPR-assisted estimation technique requires as a starting point the ability to obtain dielectric information from radar data. The sequence for implementing the proposed procedure for a bimodal system is summarized as follows:

1. Analyze velocity of surface CMP or cross-hole tomographic GPR data to estimate the dielectric constant field.

2. Identify the possible hydraulic parameters given the dielectric data and petrophysical relationships that are extracted from the literature or developed for the site of interest. We use petrophysical relationships developed by *Knoll et al.* [1995] to transfer the dielectric constants into intrinsic permeability and saturation values. For an ideal system composed of two facies, this particular relation produced two possible values of permeability ($k_1$ and $k_2$) and saturation ($S_1$ and $S_2$) at each location for each dielectric constant measurement.

3. Estimate the expected values of permeability or saturation to be used in (5), (9), or (10). These fields can be estimated using different approaches; in this study we use a fluid flow simulation to obtain $\langle S \rangle$ and a kriging technique to obtain $\langle S \rangle^c$. Our numerical case studies show that the GPR-assisted hydraulic parameter estimation procedure is not sensitive to the estimation method of $\langle S \rangle$ or $\langle S \rangle^c$.

4. Calculate the probability that the saturation ($S$) is associated with a particular facies (for example, $S = S_1$) given the dielectric constant information at that location using (9) or (10). As the probability of observing $k_1$ is the same as the probability of observing $S_1$, the calculated probability is also the probability that the intrinsic permeability at that location is $k_1$.

5. Invoke the principle of maximum likelihood to select single permeability and saturation estimates from the set of possible values at each location.

We have shown using numerical examples that even with a moderate degree of error introduced from various sources, incorporation of data potentially available from GPR with borehole data can improve the estimation of hydraulic parameters over a procedure based on borehole data alone. In particular, we find the following:

1. When information potentially available from GPR data is included in the estimation procedure, saturation estimates are improved over those estimates obtained from borehole information alone.

2. The saturation estimation is optimal when the petrophysical curves of the facies that comprise the system are similar. In our numerical case studies the curves are most similar, and thus the saturation estimate is the best in system III (Figure 4c), which also represents an environment in which GPR acquisition is likely to be successful.

3. GPR-assisted intrinsic permeability estimation is improved over the estimates obtained using well bore data alone when the petrophysical curves of the facies that comprise the systems are distinct. In the systems we investigate, this occurs when one facies is a sand with a permeability of $10^{-7}$ cm$^2$ and the permeability of the other facies is near $10^{-11}$ cm$^2$ (system I and II, Figures 4a and 4b, respectively). As added error increases and the system becomes more homogeneous, the method loses the capability to distinguish between the facies that comprise the system. However, we are generally interested in permeability estimation in heterogeneous environments, and under these circumstances the GPR-assisted permeability estimation procedure is useful provided that GPR acquisition is possible. In heterogeneous environments that are partially composed of clays, the performance of GPR methods depends on the acquisition geometry and parameters, as well as on the conditions at the site such as saturation state, type of clay present, and thickness of the clay layers.

The proposed technique extends the TDR concept of using electromagnetic signal travel times to estimate a one-dimensional profile of water content to using GPR travel times to estimate two-dimensional cross sections of both saturation and intrinsic permeability. The method should be especially advantageous in areas favorable for GPR data acquisition where detailed resolution is required, but drilling of numerous boreholes is prohibited owing to the time and cost involved as well as specific site limitations. Although collection and analysis of CMP or cross-hole GPR data are relatively new and laborious processes, and are still topics of research, this study suggests that GPR-assisted vadose zone hydraulic parameter estimation is a method worthy of further investigation.

**Acknowledgments.** This paper is part of a Ph.D. thesis to be submitted by Susan Hubbard in partial fulfillment of her degree requirements. This study was supported by the Assistant Secretary for Energy Research, Office of Health and Environmental Research, Subsurface

Science Program under U.S. Department of Energy contract DE-AC03-76SF00098 to Ernie Majer and by DE-FG07-96ER14726 and NSF EAR-9628306 to Yoram Rubin. We wish to thank three anonymous reviewers for their thoughtful comments and suggestions and Karsten Pruess for use of his TOUGH2 flow simulation code. All computations were carried out at the Center for Computational Seismology (CCS) at the Lawrence Berkeley National Laboratory.

## References

Annan, A. P., and S. Cosway, Ground penetrating radar survey design, *Proceedings of the Symposium on the Applications of Geophysics to Engineering and Environmental Problems (SAGEEP)*, Environ. and Eng. Geophys. Soc., Englewood, Colo., 1992.

Bear, J., *Dynamics of Fluids in Porous Media*, 784 pp., Elsevier, New York, 1972.

Beres, M., Jr., and F. P. Haeni, Application of ground penetrating radar methods in hydrogeologic studies, *Ground Water*, *29*(3), 375–386, 1991.

Birchak, J. R., C. G. Gardner, J. E. Hipp, and J. M. Victor, High dielectric constant microwave probes for sensing soil moisture, *Proc. IEEE*, *62*(1), 93–102, 1974.

Carrera, J., and S. P. Neuman, Estimation of aquifer parameters under transient and steady state conditions, 1, Maximum likelihood method incorporating prior information, *Water Resour. Res*., *22*(2), 199–210, 1986.

Copty, N., and Y. Rubin, A stochastic approach to the characterization of lithofacies from surface and seismic and well data, *Water Resour. Res*., *31*(7), 1673–1686, 1995.

Copty, N., Y. Rubin, and G. Mavko, Geophysical-hydrogeological identification of field permeabilities through Bayesian updating, *Water Resour. Res*., *29*(8), 2813–2825, 1993.

CRC Press, Inc., *CRC Handbook of Chemistry and Physics, 1991–1992*, 72nd ed., edited by D. R. Lide, Boca Raton, Fla., 1991.

Dagan, G., Stochastic modeling of groundwater flow by unconditional and conditional probabilities: The inverse problem, *Water Resour. Res*., *21*(1), 65–72, 1985.

Davis, J., and A. Annan, Ground-penetrating radar for high-resolution mapping of soil and rock stratigraphy, *Geophys. Prospect*., *37*, 531–551, 1989.

Delhomme, J. P., Kriging in the hydrosciences, *Adv. Water Resour*., *1*(5), 251–266, 1978.

Desbarats, A. J., Numerical estimation of effective permeability in a sand-shale formation, *Water Resour. Res*., *23*(2), 273–286, 1987.

Deutsch, C., and A. G. Journel, *GSLIB: Geostatistical Software Library and Users Guide*, 313 pp., Oxford Univ. Press, New York, 1992.

Dix, C. H., Seismic velocities from surface measurements, *Geophysics*, *20*, 68–86, 1955.

Doolittle, J. A., and M. E. Collins, Use of soil information to determine application of ground penetrating radar, *J. Appl. Geophys*., *33*, 101–108, 1995.

Elrick, D. E., and W. D. Reynolds, Infiltration from constant-head well permeameters and infiltrometers, in *Advances in Measurement of Soil Physical Properties: Bringing Theory into Practice*, *SSSA Spec. Publ*., *30*, edited by G. C. Topp and W. D. Reynolds, pp. 1–24, Soil Sci. Soc. of Am., Madison, Wis., 1992.

Fisher, E., G. McMechan, and A. P. Annan, Acquisition and processing of wide-aperture ground-penetrating radar data, *Geophysics*, *57*(3), 495–504, 1992.

Gelhar, L. W., *Stochastic Subsurface Hydrology*, Prentice Hall, Englewood Cliffs, N. J., 1993.

Ginn, T. R., and J. H. Cushman, Inverse methods for subsurface flow: A critical review of stochastic techniques, *Stochastic Hydrol. Hydraul*., *4*, 1–26, 1990.

Gomez-Hernandez, J. J., and R. M. Srivastava, ISIM3D: An ANSI-C three-dimensional multiple indicator conditional simulation program, *Comput. Geosci*., *16*, 395–440, 1990.

Green, R. E., and G. C. Topp, Survey of use of field methods for measuring soil hydraulic properties, appendix, in *Advances in Measurement of Soil Physical Properties: Bringing Theory Into Practice*, edited by G. C. Topp and W. D. Reynolds, *SSSA Spec. Publ. 30*, pp. 281–288, 1992.

Hale, D., Dip-moveout by Fourier transform, *Geophysics*, *49*, 741–757, 1984.

Hyndman, D. W., J. M. Harris, and S. M. Gorelick, Coupled seismic and tracer test inversion for aquifer property characterization, *Water Resour. Res*., *30*(7), 1965–1977, 1994.

Johnson, N. M., and S. J. Dreiss, Hydrostratigraphic interpretation using indicator geostatistics, *Water Resour. Res*., *25*(12), 2501–2510, 1989.

Kalma, J. D., and M. Sivapalan (Eds.), *Scales Issues in Hydrological Modeling*, 489 pp., John Wiley, New York, 1995.

Katsube, T. J., The critical frequency and its effect on EM propagation, *Geol. Surv. Can. Pap 75-1*, *Part A*, pp. 101–105, 1974.

Kitanidis, P., and E. G. Vomvoris, A Geostatistical approach to the inverse problem in groundwater modeling (steady state) and one-dimensional simulations, *Water Resour. Res*., *19*(3), 677–690, 1983.

Knoll, M., and R. Knight, Relationships between dielectric and hydrogeologic properties of sand-clay mixtures: *Proceedings of the Fifth International Conference on Ground Penetrating Radar*, pp. 45–61, Environ. and Eng. Geophys. Soc., Englewood, Colo., 1994.

Knoll, M. P., F. P. Haeni, and R. J. Knight, Characterization of sand and gravel aquifer using ground-penetrating radar, Cape Cod, Massachusetts, *Water Resour. Invest*., *91-4034*, pp. 29–34, 1991.

Knoll, M., R. Knight, and E. Brown, Can accurate estimates of permeability be obtained from measurements of dielectric properties?, *SAGEEP Annual Meeting Extended Abstracts*, Environ. and Eng. Geophys. Soc., Englewood, Colo., 1995.

Kutilek, M., and K. Nielsen, *Soil Hydrology*, Catena-Verlag, Cremlingen-Destedt, Germany, 1994.

Leverett, M. C., Capillary behavior in porous soils, *Trans. Am. Inst. Min. Metall. Pet. Eng*., *142*, 152–169, 1941.

Marion, D., Acoustical, mechanical and transport properties of sediments and granular materials, Ph.D. dissertation, Stanford Univ., Stanford, Calif., 1990.

Marion, D., A. Nur, H. Yin, and D. Han, Compressional velocity and porosity in sand-clay mixtures, *Geophysics*, *57*, 554–563, 1992.

Mazac, O., W. E. Kelly, and I. Landa, A hydrogeological model for relations between electrical and hydraulic properties of aquifers, *J. Hydrol*., *79*, 1–19, 1985.

Mazac, O., M. Cislerova, and T. Vogel, Applications of geophysical methods in describing spatial variability of saturated hydraulic conductivity in the zone of aeration, *J. Hydrol*., *103*, 117–126, 1988.

Mood, A. M. F., and F. A. Graybill, *Introduction to the Theory of Statistics*, 2nd ed., McGraw-Hill, New York, 1963.

Nekut, A. G., Electromagnetic ray-trace tomography, *Geophysics*, *55*, 371–377, 1994.

Pruess, K., TOUGH2—A general purpose numerical simulator for multiphase fluid and heat flow, *Lawrence Berkeley Lab. Rep. 29400*, Berkeley, Calif., 1991.

Roth, K., R. Schulin, H. Fluhler, and W. Attinger, Calibration of time domain reflectometry for water content measurement using a composite dielectric approach, *Water Resour. Res*., *26*(10), 2267, 1990.

Rubin, Y., Flow and transport in bimodal heterogeneous formations, *Water Resour. Res*., *31*(10), 2461–2468, 1995.

Rubin, Y., and G. Dagan, Stochastic identification of transmissivity and effective recharge in steady groundwater flow, 1, Theory, *Water Resour. Res*., *23*(7), 1185–1192, 1987.

Rubin, Y., and J. Gomez-Hernandez, A stochastic approach to the problem of upscaling conductivity in disordered media: Theory and unconditional numerical simulations, *Water Resour. Res*., *26*(4), 691–701, 1990.

Rubin, Y., G. Mavko, and J. Harris, Mapping permeability in heterogeneous aquifers using hydrological and seismic data, *Water Resour. Res*., *28*(7), 1192–1800, 1992a.

Rubin, Y., D. Or, and D. P. Groeneveld, Characterization of soil spatial variability for upgrading soil water monitoring in Owens Valley, California, in *Dep. of Civ. Eng. Rep. UCB/GT/92-08*, Univ. of Calif., Berkeley, 1992b.

Sanchez-Vila, X., J. P. Girardi, and J. Carrera, A synthesis of approaches to upscaling of hydraulic conductivities, *Water Resour. Res*., *31*(4), 867–882, 1995.

Scheidegger, A. E., *The Physics of Flow Through Porous Media*, 3rd ed., Univ. of Toronto Press, Toronto, 1974.

Schlesinger, W. H., J. F. Reynolds, G. L. Cunningham, L. F. Huenneke, W. M. Jarrell, R. A. Virginia, and W. G. Whitford, Biological feedbacks in global desertification, *Science*, *24*, 1043–1048, 1990.

Sena, A. G., and M. N. Toksoz, Simultaneous reconstruction of permittivity and conductivity for crosshole geometries, *Geophysics*, *55*(10), 1302–1311, 1990.

Sheets, K. R., and J. M. H. Hendrickx, Noninvasive soil water content measurement using electromagnetic induction, *Water Resour. Res*., *31*(10), 2401–2409, 1995.

Shen, L. C., W. C. Savre, J. M. Price, and K. Athavale, Dielectric properties of reservoir rocks at ultra-high frequencies, *Geophysics*, *50*, 692–714, 1985.

Smith, D. G., and H. M. Jol, Ground-penetrating radar investigation of a Lake Bonneville Delta, Provo level, Bringham City, Utah, *Geology*, *20*, 1083–1086, 1992.

Steeples, D., and R. Miller, Seismic reflection methods applied to engineering, environmental, and groundwater problems, in *Geotechnical and Environmental Geophysics*, vol. 1, edited by S. Ward, pp. 1–30, Soc. of Explor. Geophys., Tulsa, Okla., 1990.

Sun, N. Z., *Inverse Problems in Groundwater Modeling*, Kluwer Acad., Norwell, Mass., 1994.

Tillard, S., and J. Dubois, Analysis of GPR data: Wave propagation and velocity determination, *J. Appl. Geophys*., *33*, 77–91, 1995.

Topp, G. C., J. L. Davis, and A. P. Annan, Electromagnetic determination of soil water content: Measurements in coaxial transmission lines, *Water Resour. Res*., *16*(3), 574–582, 1980.

Ulriksen, C. P. F., Application of impulse radar to civil engineering, Ph.D. dissertation, Lund Univ. of Technol., Lund, Sweden, 1982.

van Genuchten, M. T., A closed-form equation for predicting the hydraulic Conductivity of unsaturated soils, *Soil Sci. Soc. Am. J*., *44*, 892–898, 1980.

Ward, S. (Ed.), *Geotechnical and Environmental Geophysics*, *Soc. of Explor. Geophys. Ser., Invest. in Geophys*., vols. I, II, and III, Soc. of Explor. Geophys., Tulsa, Okla., 1990.

Wharton, R. P., G. A. Hazen, R. N. Rau, and D. L. Best, Electromagnetic propagation logging: Advances in technique and interpretation, *Soc. Pet. Eng. Pap. 9267*, 1980.

Wyatt, D. E., M. G. Waddell, and G. B. Sexton, Geophysics and shallow faults in unconsolidated sediments, *Ground Water*, *34*(2), 326–334, 1996.

Yeh, W., Review of parameter identification procedures in groundwater hydrology: The inverse problem, *Water Resour. Res*., *22*(2), 95–108, 1986.

Yilmaz, O., *Seismic Data Processing*, *Soc. of Explor. Geophys. Ser., Invest. in Geophys*., vol. 2, Soc. of Explor. Geophys., Tulsa, Okla., 1987.

Yin, H., Acoustic velocity and attenuation of rocks, Ph.D. dissertation, Stanford Univ., Stanford, Calif., 1993.

---

S. S. Hubbard and Y. Rubin, Department of Civil and Environmental Engineering, University of California, Berkeley, CA 94720. (e-mail: shubbard@ccs.lbl.gov)

E. Majer, Earth Science Division, Lawrence Berkeley National Laboratory, Berkeley, CA 94720.

(Received August 12, 1996; revised December 1, 1996;
accepted December 23, 1996.)